Supporting information for: Heterogeneous Photon Recycling and Charge Diffusion Enhance Charge Transport in Quasi-2D Lead-Halide Perovskite Films

Silvia G. Motti,[†] Timothy W. Crothers,[†] Rong Yang,[‡] Yu Cao,[‡] Renzhi Li,[‡] Michael B. Johnston,[†] Jianpu Wang,[‡] and Laura M. Herz[*,†]

[†]*Department of Physics, University of Oxford, Clarendon Laboratory, Parks Road, Oxford OX1 3PU, United Kingdom*

[‡]*Key Laboratory of Flexible Electronics (KLOFE) & Institute of Advanced Materials (IAM), Jiangsu National Synergetic Innovation Center for Advanced Materials (SICAM), Nanjing Tech University (NanjingTech), 30 South Puzhu Road, Nanjing 211816, China*

E-mail: laura.herz@physics.ox.ac.uk

Contents

1 Experimental Section

1.1 Sample Preparation

3BBAI, MACl and PbI_2 with molar ratio of 2.0:2.7:3 were dissolved in DMF at a weight concentration of 20% and stirred overnight in a nitrogen-filled glovebox before use.

For the spectroscopic measurements described in this study, a 2 mm-thick z-cut quartz substrate was used to support the perovskite film. The substrate was placed on a hotplate at the temperature of 140 °C for 2 – 3 minutes, then 40 μL perovskite precursor solution was immediately deposited onto 140 °C substrate and spin-coated at 5000 rpm for 20 seconds.

The perovskite film was post-annealed for 15 min on a hotplate maintained at 90 °C.

A Dektak 150 surface profilometer was used to determine the film thickness as 452±18 nm.

1.2 STEM

The cross sectional STEM image shown in Figure 1 of the main manuscript was collected on a FEI Titan G2 80200 ChemiSTEM operated at 200 keV. To avoid electronic charging, a perovskite film deposited in the same way as outlined above was incorporated into a full device stack, as described in detail previously.[S1] Briefly, a 20-nm thick layer of PEDOT was deposited by spin-coating on top of a 1.1-mm thick ITO-coated glass substrate, followed by hot-casting of a perovskite film as described above, and spin-coating of a 90-nm thick PCBM film, topped with a metal (Cr/Al) electrode.

1.3 Steady-State Absorption

Reflection and transmission spectra were measured using a Bruker 80v Fourier-transform infrared spectrometer with a tungsten halogen lamp source, a CaF beamsplitter and a silicon diode detector. Data was collected with a resolution of 4 cm^{-1}. A silver mirror was used as reflection reference and a blank quartz substrate was used as transmission reference.

The reflectivity spectra were obtained from the measurement of reflected light from the front and back of the mixed quasi-2D/3D perovskite film with the silver mirror reflection measurement as reference. The reflectivity values were used to account for reflection losses of the photoexcitation in further experiments and correctly estimate the charge-carrier density.

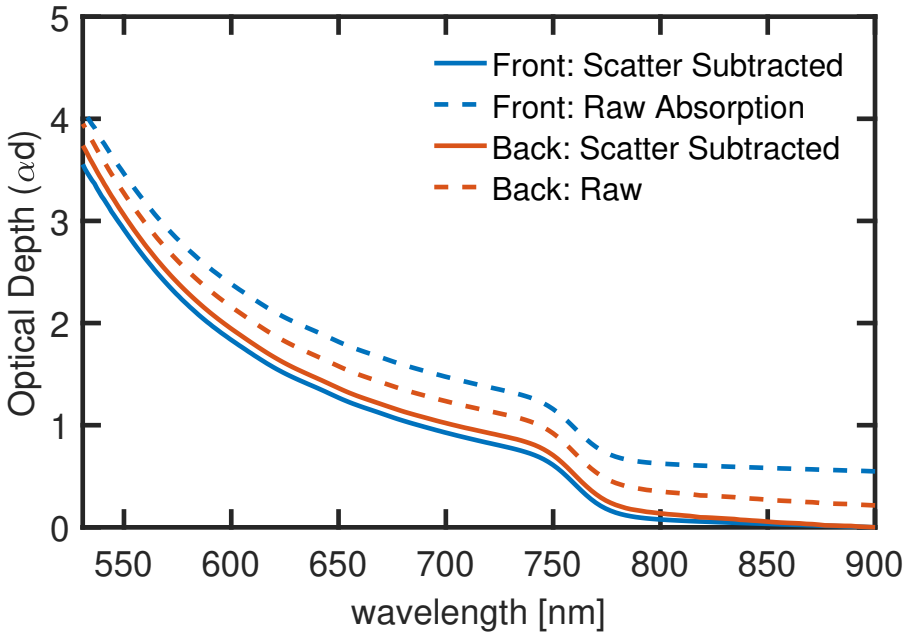

Figure S1: Absorption spectrum of the mixed quasi-2D/3D perovskite film. Dotted lines show the raw data while solid lines show the same data with a correction for background scatter done by removing the average amplitude in the range 850 nm–950 nm.

Figure S1 shows the absorption spectrum of the mixed quasi-2D/3D perovskite film, both with and without a correction for background scatter. The approximated contribution of light scattering was calculated based on the average sub-gap absorption in the range 850 nm–950 nm. This value was subtracted from the entire spectrum to obtain a scatter-corrected absorption spectrum.

1.4 Steady-State and Time-Resolved Photoluminescence

The excitation source was a 398 nm pulsed diode laser (PicoHarp, LDHDC405M) operating at 500 kHz. Such a wavelength of excitation light is strongly absorbed by the perovskite film, as shown by the Beer's Law profile in Figure S2, calculated from the absorbance values

obtained experimentally for the films studied.

The PL was collected in reflection geometry and coupled into a grating spectrometer (Princeton Instruments, SP2558). Steady-state spectra were acquired with an iCCD (PI-MAX4, Princeton Instruments) and time-resolved measurements were acquired in a Time Correlated Single Photon Counting (TCSPC) system (PicoHarp300). The measurements were performed under vacuum (pressure $<10^1$ mbar).

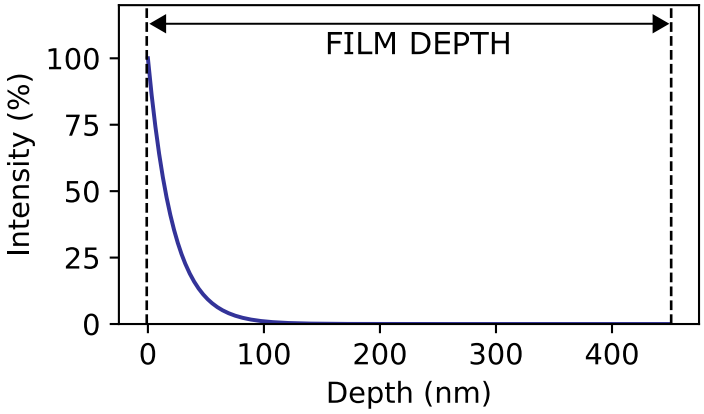

Figure S2: Attenuation profile of the excitation light (398 nm) used in PL experiments on perovskite thin films, where depth=0 is the illuminated surface and the dashed lines represent the front and back limits of the film. Due to the strong absorption coefficient of the perovskite, most of the photoexcited charge carriers are concentrated within the first 100 nm from the illuminated surface.

1.5 Optical-Pump Terahertz-Probe (OPTP) Spectroscopy

Optical-Pump THz-Probe (OPTP) measurements were performed using a Spectra Physics Mai Tai-Empower-Spitfire Pro Ti:Sapphire regenerative amplifier. The amplifier generates 35 fs pulses centered at 800 nm at a repetition rate of 5 kHz. The optical pump excitation was obtained by frequency doubling the fundamental laser output through a BBO crystal, resulting in 400 nm pulses. THz probe pulses were generated by a spintronic emitter which was composed of 1.8 nm of $Co_{40}Fe_{40}B_{20}$ sandwiched between 2 nm of Tungsten and 2 nm of Platinum, all supported by a quartz substrate. Detection of the THz pulses was performed

using electro-optic sampling in a ZnTe crystal (0.2 mm (110)-ZnTe on 3 mm (100)-ZnTe). The FWHMs of the beams for the pump and THz pulses at the sample were measured to be 1.8 mm and 0.7 mm respectively. The sample, THz emitter and THz detector were held under vacuum ($<10^{-2}$ mbar) during the measurements.

The effective charge-carrier mobility was extracted from the OPTP data using the method previously described by Wehrenfennig et al.[S2] In brief, the sheet photo-conductivity, ΔS, of a material with a thickness much shorter than the wavelength of the THz radiation can be expressed as

$$\Delta S = -\epsilon_0 c(n_a + n_b)(\frac{\Delta T}{T}) \tag{1}$$

where n_a and n_b are the THz refractive indices of the materials interfacing the perovskite layer at the front and rear respectively. The quantity $\Delta T/T$ is the ratio of the photo-induced change in THz electric field to the transmitted THz electric field in the dark. The initial number of photo-excited charge carriers N is given by

$$N = \phi\frac{E\lambda}{hc}(1 - R_{pump})(1 - T_{pump}) \tag{2}$$

with E being incident pump pulse energy, λ the excitation wavelength, ϕ the ratio of free charges created per photon absorbed, and R_{pump} and T_{pump} being the reflected and transmitted fractions of the pump beam. These two equations can be used to extract the charge-carrier mobility μ through

$$\mu = \frac{\Delta S A_{eff}}{Ne} \tag{3}$$

where A_{eff} is the effective area from the overlap of the pump and probe beams and e is the elementary charge. Substituting Equations 1 and 2 into Equation 3 we obtain

$$\phi\mu = -\frac{\epsilon_0 c(n_a + n_b)(A_{eff})}{Ne\lambda(1 - R_{pump})(1 - T_{pump})}(\frac{\Delta T}{T}) \tag{4}$$

from which the effective charge-carrier mobility $\phi\mu$ may be determined based on the pump

beam parameters and the initial measured $\Delta T/T$ of the sample. Here, μ is the charge-carrier mobility, and ϕ is the charge-to-photon branching ration which is assumed to be unity at room temperature for $MAPbI_3$.

Charge-carrier mobility values for each side of the film were calculated based on the average of at least 10 measurements taken from 3 identical samples.

2 Photoluminescence Lifetimes

Time-resolved photoluminescence spectra were fitted as two Gaussian components with distinct lifetimes. The PL as a function of time (t) and wavelength (λ) was modelled as:

$$I_{PL}(t,\lambda) = A_1 \cdot e^{-\frac{(\lambda-\lambda_1)^2}{2w_1^2}} \cdot e^{-t/\tau_1} + A_2 \cdot e^{-\frac{(\lambda-\lambda_2)^2}{2w_2^2}} \cdot e^{-t/\tau_2} \tag{5}$$

where A_1 and A_2 are the amplitudes, w_1 and w_2 the bandwidths, λ_1 and λ_2 the central wavelengths and τ_1 and τ_2 the lifetimes of each component in the emission.

Experimental data together with fits produced by the model can be seen in Figures S3 and S4. Figure S3 shows the case where the front side of the sample is excited, while Figure S4 shows the case where where the back side of the sample is excited. In each case, PL was collected in reflection geometry from the same side on which the film was excited.

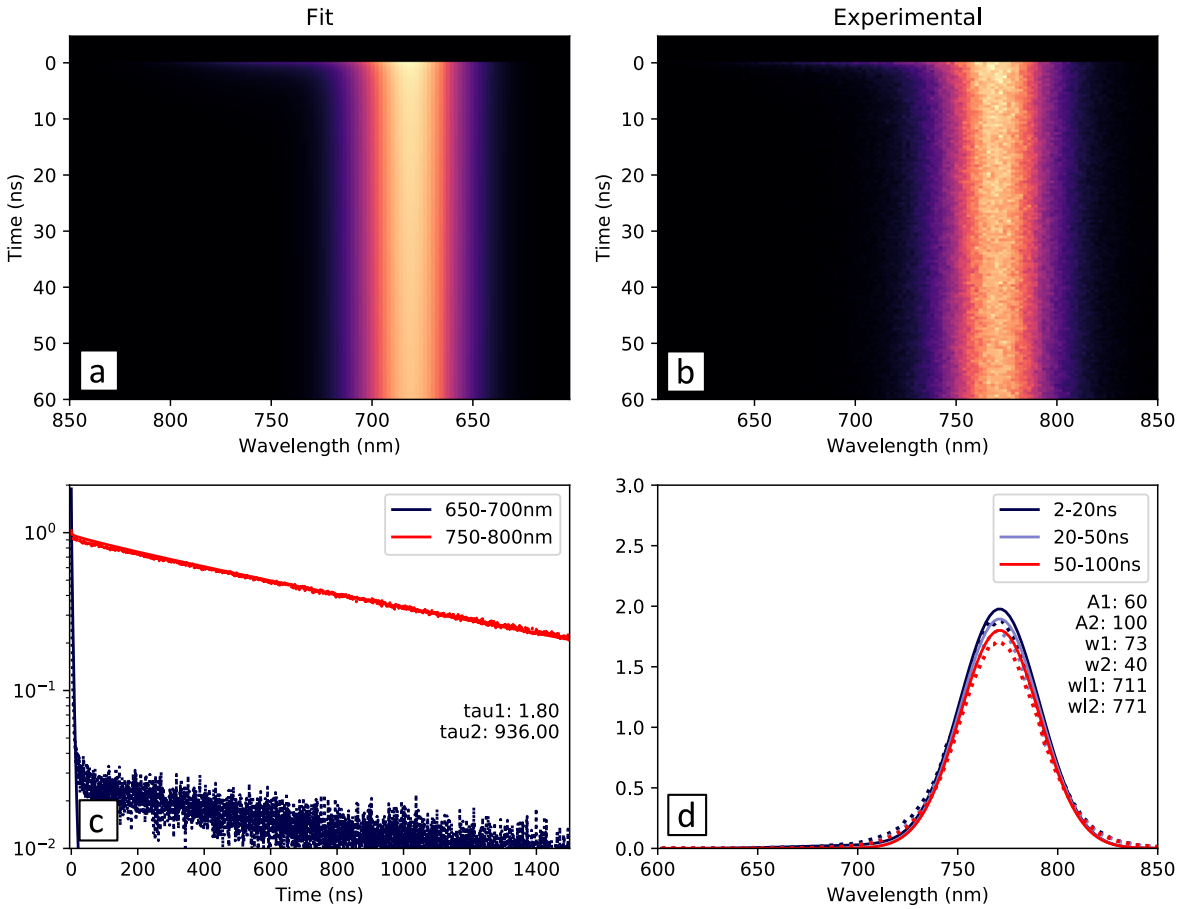

Figure S3: a,b) Fitted model and experimental data of time-resolved photoluminescence spectra taken using a photoexcitation wavelength of 398 nm, from the front of the mixed quasi-2D/3D perovskite film; c) Dynamic profiles integrated in the spectral intervals 650-700 nm (dark blue) and 750-800 nm (red), dotted lines are experimental data and solid lines are fitted curves; d) Spectral profiles integrated over three different time intervals, dotted lines are experimental data and solid lines are fitted curves.

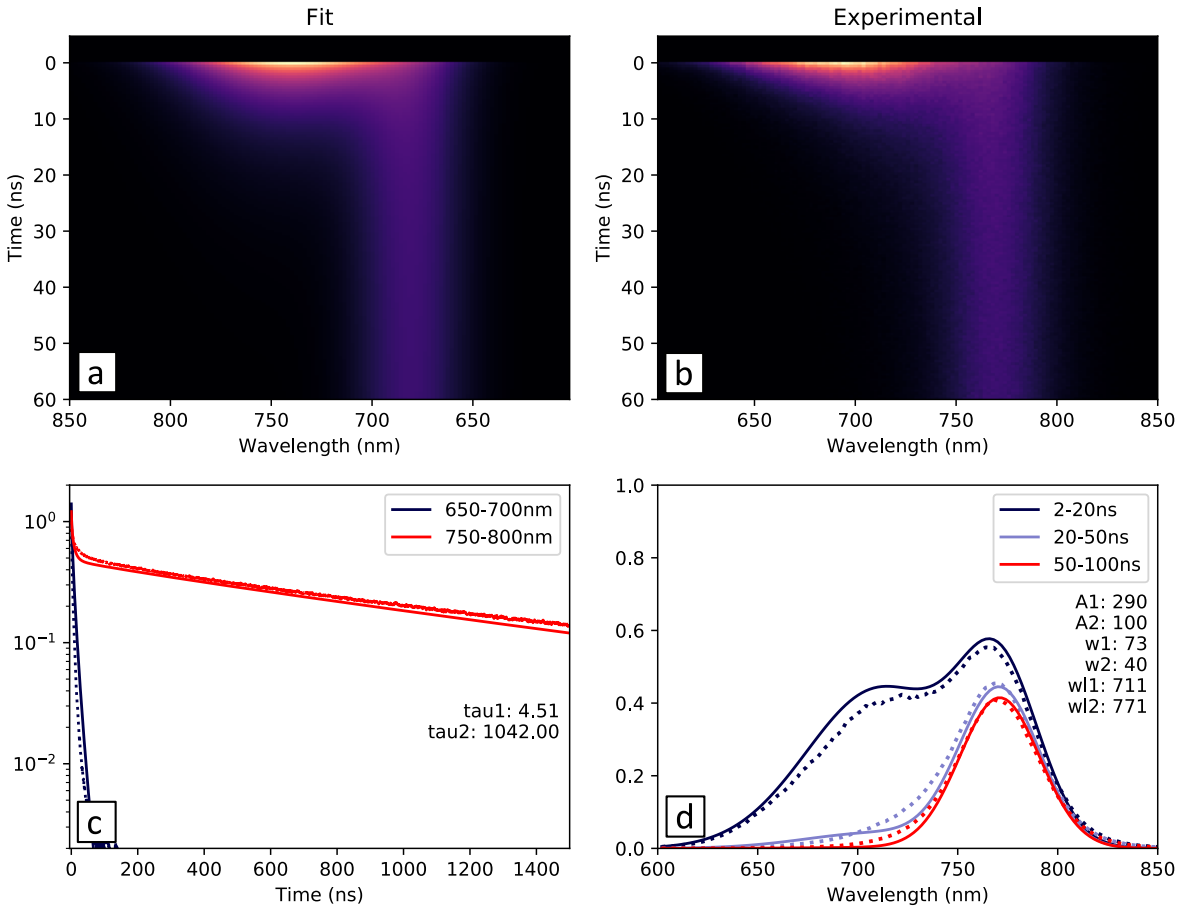

Figure S4: a,b) Fitted model and experimental data of time-resolved photoluminescence spectra taken using a photoexcitation wavelength of 398 nm, from the back (substrate side) of the mixed quasi-2D/3D perovskite film; c) Dynamic profiles integrated in the spectral intervals 650-700 nm (dark blue) and 750-800 nm (red), dotted lines are experimental data and solid lines are fitted curves; d) Spectral profiles integrated over three different time intervals, dotted lines are experimental data and solid lines are fitted curves.

3 OPTP Dynamics

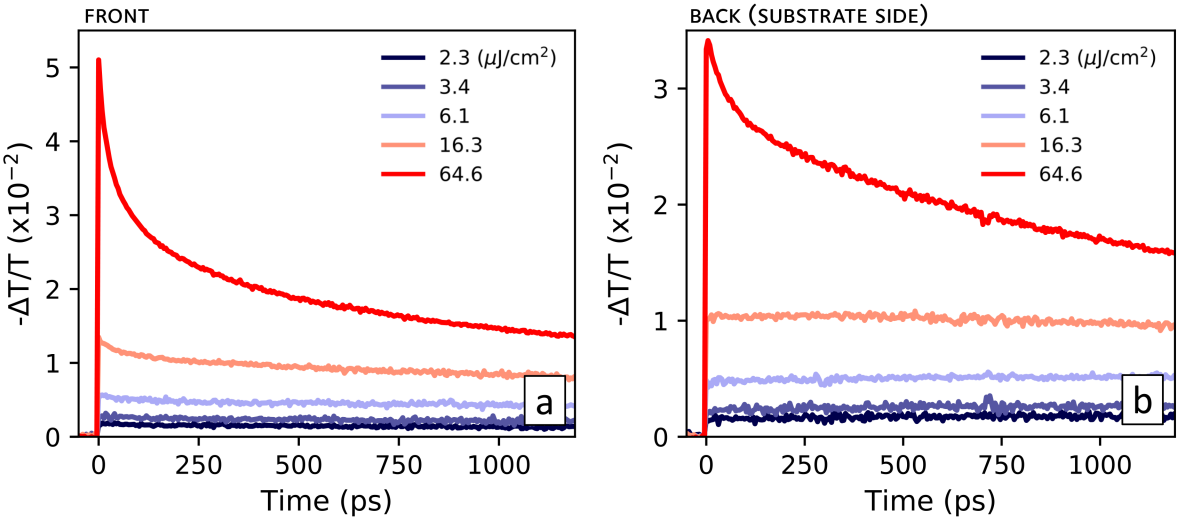

Figure S5: OPTP dynamics taken with photoexcitation from the front (a) or back (b) side of the film. Excitation was performed at a wavelength 400 nm with 35-fs pulses at a repetition rate of 5 kHz.

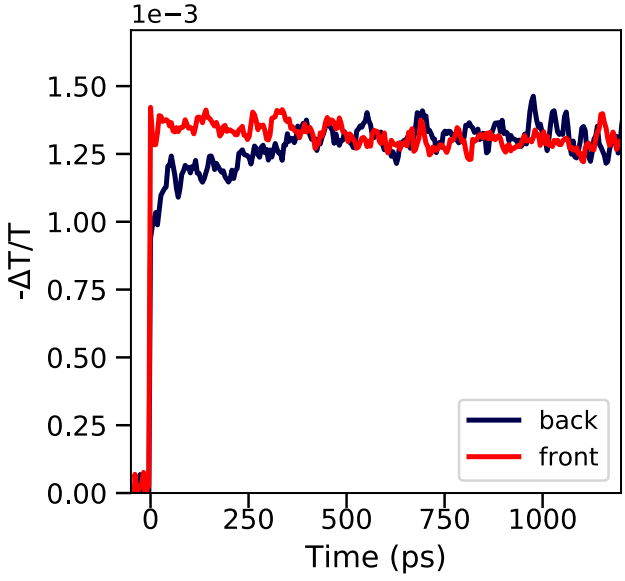

Figure S6: OPTP dynamics taken with photoexcitation on the front (red) or back (black) side of the mixed quasi-2D/3D perovskite film, at fluence $\sim 2\,\mu J\,cm^{-2}$. Excitation was performed at wavelength 400 nm with a 35 fs pulses at a repetition rate of 5 kHz.

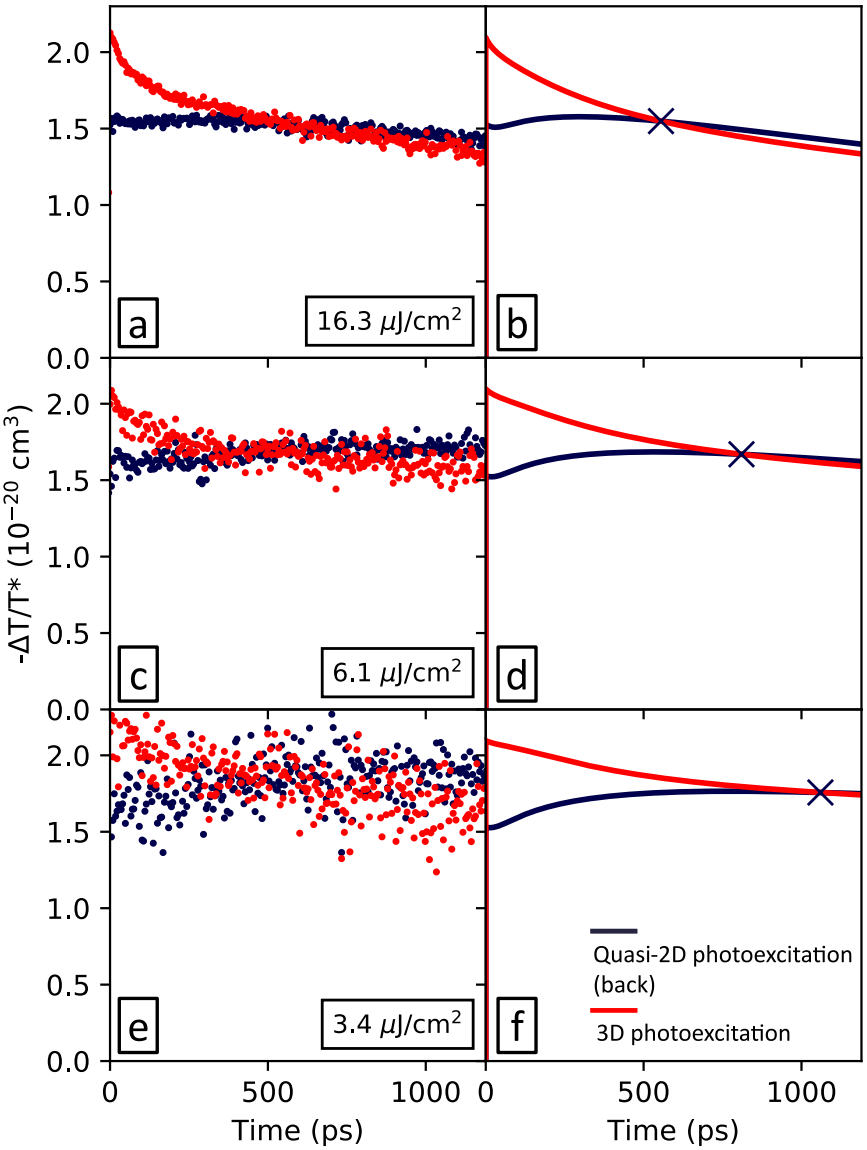

Figure S7: Superimposed OPTP dynamics taken when photoexciting the mixed quasi-2D/3D perovskite film from the front (red) or back (dark blue) side, at fluences of 3.4 , 6.1 , and 16.3 µJ cm^{-2}. Dots in panels (a), (c) and (e) are experimental data and the solid lines in (b), (d) and (f) are simulated transients obtained with diffusion and reabsorption being accounted for. Data scaled as $\Delta T/T^* = (\Delta T/T)/N_0$, where N_0 is the predicted initial density of photoexcited carriers. Simulated transients in (b), (d) and (f) were obtained from a fixed value of N_0 on both sides.

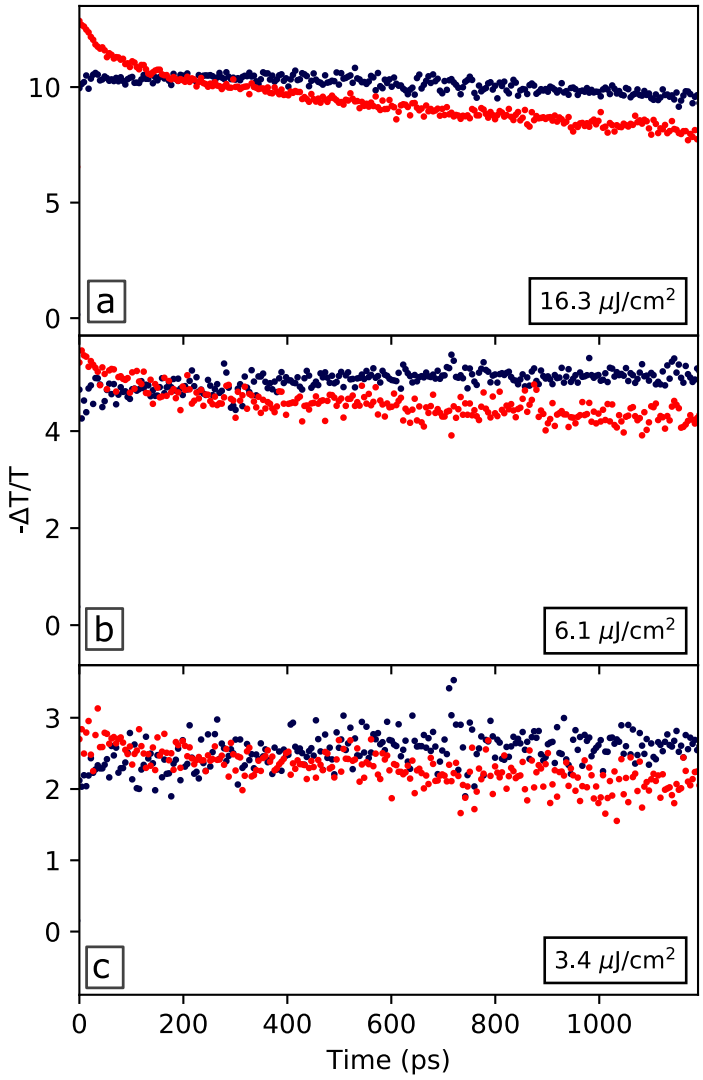

Figure S8: Superimposed OPTP dynamics taken when photoexciting the mixed quasi-2D/3D perovskite film from the front (red) or back (dark blue) side, at fluences of 3.4 , 6.1 and 16.3 µJ cm^{-2}. Raw ΔT/T data (not scaled) in units of 10^{-3}.

4 Modelling Charge-Carrier Dynamics in Quasi-2D/3D Sample

This section describes how the charge-carrier dynamics in the mixed quasi-2D/3D perovskite film investigated in this study are modelled. First, we describe a model of the mixed quasi-2D/3D perovskite film structure, dividing the perovskite film into two different regions based on experimental characterization. The rest of this section will describe in more detail how the charge-carrier dynamics of the mixed quasi-2D/3D perovskite film are simulated. This will include a description of how the simulations account for the different charge-carrier mobilities and PL spectra in the two regions. After we have described the simulations, the absorption and photoluminescence (PL) spectra of the sample are then investigated and used to understand photon reabsorption and the effect of heterogeneous PL emission in the mixed quasi-2D/3D perovskite film.

4.1 Model Used for the Perovskite Film

Here, a simple model is developed that reflects the structure of the mixed quasi-2D/3D perovskite film. Two different regions of the film are identified using film profilometry and cross-sectional STEM to identify the different extents of the two regions.

Modelling the Mixed 2D/3D Film as Two Regions The mixed quasi-2D/3D perovskite film contains both quasi-2D and 3D perovskite domains, so it is necessary to split the film into different regions based on the types of domains present. Figure 1a) in the main text shows a STEM image of the cross-section of a mixed quasi-2D/3D perovskite film, where both 3D and quasi-2D domains can be seen. Close to the substrate the sample contains large fractions of quasi-2D domains, while near the surface mainly 3D perovskite domains are present.

For the purposes of modelling the charge-carrier dynamics, the film is considered as

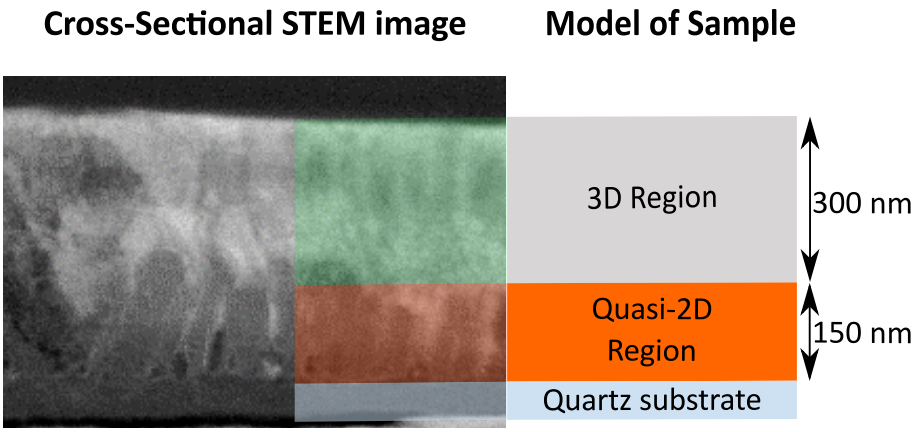

Figure S9: Schematic representation of the mixed quasi-2D/3D perovskite film; the left part of the figure shows the STEM image taken for a perovskite film incorporated into a device stack (from Figure 1a) of the main text), while the right side shows the simplified model of the film used for simulating the charge-carrier dynamics. It can be seen in the STEM image how the film is divided into two regions with different morphologies. The overall thickness of 450 nm is assigned from the surface profilometry data taken on a film deposited on z-cut quartz which is examined in the spectroscopic measurements.

comprising of two layers (representing the quasi-2D and 3D regions), stacked on top of one another. Figure S9 shows how surface profilometry and the STEM image of the perovskite film are used to build this simplified model. The bottom of the film is modelled as a quasi-2D region, representing the mix of quasi-2D and 3D perovskite domains seen at the bottom of the STEM image. The rest of the film is represented as a capping layer of pure 3D perovskite.

Since electron microscope images need the presence of a conductive substrate to avoid sample charging, while the THz photoconductivity measurements require the use of a substrate that is transparent to THz radiation (here z-cut quartz), this meant that the two measurements had to be taken on films prepared on different substrates. We verified that the shape of the transmission spectra assocated with the perovskite film was unaffected by the change in substrate, meaning that the thickness ratio of the quasi-2D and 3D perovskite regions should be unchanged by the difference in substrate. Thus, to account for slight differences in film thickness between the two mixed quasi-2D/3D perovskite films, we scaled the cross-sectional STEM image taken for the film inside the device stack to reflect the thickness of the film deposited on z-cut quartz (∼450 nm, as measured by surface profilometry).

Figure S9 shows the STEM image with the vertical film thickness assigned to 450 nm accordingly. From such scaling, we deduce the average thickness of each layer as 150 nm for the quasi-2D region and 300 nm for the 3D region. In this way, the mixed quasi-2D/3D perovskite film can be represented by the simplified model on the left of Figure S9, consisting of a quasi-2D and a 3D region.

Properties of the two regions Having split the sample into two regions, we analyze their distinct properties. Although, in reality, there is no sharp distinction between the regions, using light with short penetration depth, the volume of the mixed quasi-2D/3D perovskite film corresponding to each region can be independently probed. This means that separate properties can be assigned to each of the modelled regions, namely the charge-carrier mobility and PL spectrum.

Both of these measurements are made by exciting either the front or the back of the mixed quasi-2D/3D perovskite film with light at 400 nm. From Figure S1 it can be seen that even at 550 nm excitation the perovskite absorbs light strongly enough such that $1/\alpha_{pump} < 100$ nm. However, due to the strong absorption of the sample at the pump wavelength of 400 nm, the absorption depth at this wavelength could not be determined. Instead, the previously reported[S3] value of $\alpha_{pump} = 2 \times 10^5\,\mathrm{cm}^{-1}$ ($1/\alpha_{pump} < 50$ nm), for a $MAPbI_3$ film was used since the 3D phase perovskite is dominant in the absorption spectrum of the mixed quasi-2D/3D perovskite film. Therefore, for an excitation at a wavelength of 400 nm, all of the light will be absorbed before reaching the modelled boundary between the two regions (see absorption profile in Figure S2). The generated charge carriers can then be assumed to all be in one of the two regions. For this reason, when the front side of the mixed quasi-2D/3D perovskite film is excited, the measurement is associated with the 3D region, and when the back side is excited, the measurement is associated with the quasi-2D region.

OPTP spectroscopy was used to measure the charge-carrier mobility of the mixed quasi-2D/3D perovskite film. Exciting the film from the front side, the charge-carrier mobility

was measured as $23.9\,\mathrm{cm^2\,V^{-1}\,s^{-1}}$. This was taken as the charge-carrier mobility for the 3D region of the sample. Similarly, when exciting the sample on the back side (through the substrate), the charge-carrier mobility was measured as $17.4\,\mathrm{cm^2\,V^{-1}\,s^{-1}}$. This value was used as the charge-carrier mobility in the quasi-2D region.

The PL spectrum was also measured for excitation from each side of the mixed quasi-2D/3D perovskite film using an excitation wavelength of 398 nm, which has a similar absorption coefficient. Figures S3 d) and S4 d) respectively show the PL spectra for the cases where the front and back side of the mixed quasi-2D/3D perovskite film are excited. The spectra considered were taken from the early-time emission (0 – 20 ns). The model considers the emission of quasi-2D region as described by the PL spectrum measured for excitation of the back of the film, while the 3D region is characterized by the emission spectrum measured when exciting the front side of the film.

In summary, a simple model of the mixed quasi-2D/3D perovskite film has been described. The film is modelled as two layers of perovskite, with the top being composed of 3D perovskite domains and the bottom as a quasi-2D layer. The model assumes that each region is identical, except for their thickness, charge-carrier mobility and PL spectrum.

4.2 Description of Dynamical Model

In this section the details of the dynamical model used to simulate the charge-carrier dynamics in the mixed quasi-2D/3D perovskite film are described. As discussed in the previous section, the mixed quasi-2D/3D perovskite film is modelled as two separate regions, with different charge-carrier mobilities and PL spectra. The discussion here will outline how these differences between the two regions are supported by the dynamical model.

The purpose of the dynamical model is to simulate the THz photoconductivity decays measured for the mixed quasi-2D/3D perovskite film using OPTP spectroscopy. It is required that the model accounts not only for charge-carrier recombination, but additionally for charge-carrier transport by diffusion and photon reabsorption. Transport of charge carriers

is important here, as it has been previously reported that exchange of charge carriers between the quasi-2D and 3D regions is an important aspect of the charge-carrier dynamics[S4]. In this study the self-absorption model previously developed in reference [S3] was used to model the charge-carrier dynamics, as it accounts for charge-carrier recombination, diffusion and photon reabsorption. However, in order to model the charge-carrier dynamics in the mixed quasi-2D/3D perovskite film the dynamical model has been extended to allow the charge-carrier mobility, recombination rates and PL emission spectra to vary through the film. The original self-absorption model, along with the adaptations made to account for film heterogeneity will now be described.

Description of the Self-Absorption Model. Within the self-absorption model the governing equation for the charge-carrier dynamics is:

$$\frac{\partial n}{\partial t} = D\frac{\partial^2 n}{\partial z^2} + G - k_3 n^3 - k_2 n^2 - k_1 n. \tag{6}$$

where n is the charge carrier density, and k_1, k_2 and k_3 are the first, second and third order recombination constants respectively. The first term accounts for charge-carrier diffusion and the second term is the charge-carrier generation rate, which includes photon reabsorption. This equation combines the usual recombination equation for free-charge carriers with two charge-carrier transport processes, allowing the effects of charge-carrier movement on the recombination dynamics to be simulated.

In order for charge-carrier transport to occur, the model must account for a spatial variation of n inside the perovskite film. Generally n can vary across all three spatial dimensions inside the film, however, in OPTP experiments it can be considered to vary only through the film depth. This simplification can be made since the area photoexcited by the pump beam is much larger than that measured by the THz probe beam. The THz probe measures n only in the centre of the photoexcited area, and across the probed area the excitation power of the pump beam is uniform. Consequently, the self-absorption model

assumes that n only varies through the depth of a sample. Since the variation in n is one-dimensional (1D), the self-absorption model represents a perovskite film as a series of slabs, which have different n. This is illustrated in the left half Figure S10, where n at the different depths in the film is represented by an array of values.

Initially n will vary through the depth of the film because of the absorption profile of the pump-beam, however, over time, the charge-carrier transport processes will also affect the charge-carrier distribution. As n is a 1D array, the self-absorption model formulates both charge-carrier diffusion and photon reabsorption as matrices. Each element of the matrices defines how a transport process redistributes charge carriers between a given pair of points in the film. Diffusion is implemented using a forward Euler method, while photon reabsorption is calculated using a ray-tracing model, which simulates the emission and recapture of photons by the lead-halide perovskite material.

Equation 6 is solved by a finite difference method, and evolved over the same time which the OPTP experiment records. The experimental THz photoconductivity is linked to the model by summing the calculated THz photoconductivity produced by each slice in the model:

$$\left(\frac{\Delta T}{T}\right) = -\sum_j \frac{\mu e d_j}{\epsilon_0 c(c)} n_j \tag{7}$$

where d is the slice thickness and $\mathrm{n_a}$ and $\mathrm{n_b}$ are the THz refractive indices of the materials to either side of the perovskite. In this way the evolution of charge carriers in a perovskite film, under charge-carrier recombination, diffusion and photon reabsorption can be modelled, and fitted against experimental THz photoconductivity transients.

Extending the Self-Absorption Model for the Mixed 2D/3D Perovskite. Section 4.1 discussed how the mixed quasi-2D/3D perovskite film can be modelled as consisting of two different regions – a quasi-2D region and a 3D region. The two regions each have a different charge-carrier mobility and PL spectrum, which required the original model to be extended, to allow these properties to vary through the film depth. As the original self-

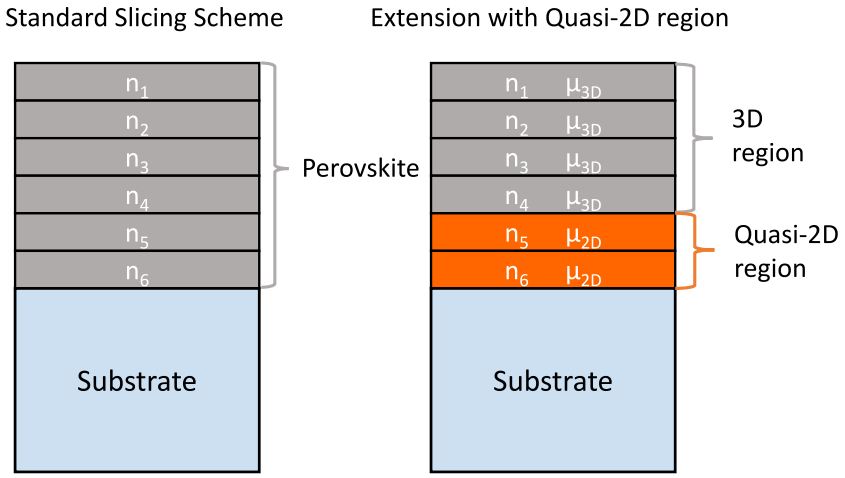

Figure S10: A schematic showing the slicing scheme used to split a perovskite layer into slabs with independent charge-carrier density. Also shown is the extension of this scheme to include a separate quasi-2D region with a different charge-carrier mobility to the 3D region.

absorption model is based around matrix operations, these changes can be supported in a straightforward manner, by replacing single values with arrays.

In the adapted version of the model presented here, each of the slices in the model has not only a unique charge-carrier density but its own charge-carrier mobility and PL emission spectrum. This updated situation is shown for the current mixed quasi-2D/3D perovskite film, on the right-hand side of Figure S10.

Although only simple changes were made to the code, they have several interesting effects. The obvious effect of having a changing charge-carrier mobility throughout the sample is that charge-carrier diffusion will happen at different rates in different locations. The more subtle effect is that, since the THz photoconductivity in Equation 7 depends on the charge-carrier mobility, if charge carriers move from a low to high mobility region the THz photoconductivity will increase. These diffusion-related effects are explored in more detail in Section 6.1. Having a different PL spectrum for each region will mean that the photons emitted from each region have different probabilities of being reabsorbed. The effects of this heterogeneous PL spectrum on the charge-carrier dynamics are discussed in Section 6.2.

4.3 Correction of the PL Spectrum for Self-Absorption

This section describes how photon reabsorption is modelled in the mixed quasi-2D/3D perovskite film, using a ray-tracing model. This model is then used to correct the PL spectra from the perovskite sample for photon reabsorption.

Description of Ray-Tracing Model Photon-reabsorption within the mixed quasi-2D/3D perovskite film is calcuated using an explicit ray tracing model, as developed in reference [S3] and summarised here.

The ray-tracing program splits the perovskite layer into slices, as discussed in Section 4.2. Propagation of PL from a given slice is simulated, using Beer's law to determine how much PL is re-absorbed in each of the other slices. This process is illustrated in Figure S11. Reflections at the perovskite boundaries are calculated using a transfer matrix model.

Ray tracing continues until either a specified fraction of the emitted light is absorbed, or the maximum propagation distance is reached. The maximum distance of coherent propagation is limited by scattering, which is experimentally determined for each sample, based on the level of sub-gap absorption (as shown in Section 1.3). After this distance is travelled, the model assumes any remaining light intensity will not be absorbed. In this way, emitted intensity is either reabsorbed by one of the perovskite slices, out-coupled through one of the interfaces or unabsorbed.

Although the simulation is 1D, the emission angle of PL in the material is still important. The angle determines the path length travelled by the ray through each slice, as well as the reflection coefficients at the perovskite boundaries. Distance travelled parallel to the film surface is not otherwise important, as the 1D slabs used in the model are uniformly photo-excited across an area much greater than the distance PL can travel in the model. This means there is no net flux of photons parallel to the film surface and any photon travelling laterally in one direction will be compensated by another photon travelling in the opposite direction.

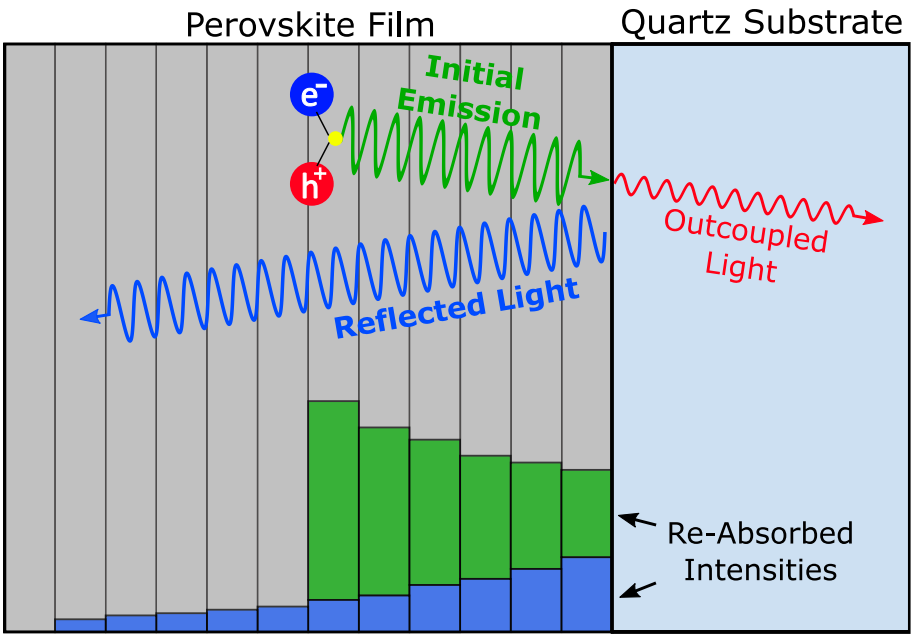

Figure S11: An illustration of the ray-tracing model used to model photon reabsorption, showing how emitted light is re-absorbed by the perovskite sample. The top of the figure shows the path of a modelled light ray through the film including reflection and out-coupling at the substrate/perovskite boundary. The lower portion of the figure shows how the intensity of the light ray is reabsorbed by each slice in the film, showing separately the contributions from each stage of the ray's path, to and from the film boundary.

Using this ray tracing procedure, the fraction of PL emitted from a given slice, at a particular emission angle and wavelength, which ends up being absorbed by each other slices can be determined.

Correction of the PL Spectra of the Mixed Quasi-2D/3D Perovskite Film Using the ray-tracing model described above, the amount of photon reabsorption in the mixed quasi-2D/3D perovskite film was calculated for wavelengths between 600 nm and 850 nm. For each wavelength, the ray-tracing model was used to simulate isotropic emission in each slice of the model outlined in Section 4.1. This procedure determines the amount of photon reabsorption at each wavelength, as well as the probability that PL will escape from the film.

Using this wavelength dependent probability that an emitted photon will escape the film, the externally measured PL spectra can be corrected for self-absorption. Figure S12 shows this correction for excitation from each side of the sample. It can be seen that after the correction, both spectra are blue-shifted, as expected. Also, the short wavelength component of the quasi-2D PL is strongly enhanced after the correction compared to the 3D band-edge emission. This can be understood from the overlap of the PL with the absorption spectra. Because the short wavelength component of the quasi-2D PL is emitted above the absorption edge, whereas the longer wavelength component is not, it is more strongly reabsorbed. This means that, when considering how much of each component was emitted, the short wavelength component must initially be much stronger. After accounting for this reabsorption, the 700 nm component is seen to dominate the PL spectrum of the quasi-2D region.

Modelling Photon-Reabsorption in the Mixed Quasi-2D/3D Perovskite Film Using the internal PL spectra for each region, a reabsorption matrix for the mixed quasi-2D/3D perovskite film was created. The corrected PL spectrum for each region is used as the modelled emission from each of the slices in the model of the mixed quasi-2D/3D perovskite film. The absorption of each wavelength is determined by the ray-tracing model, as

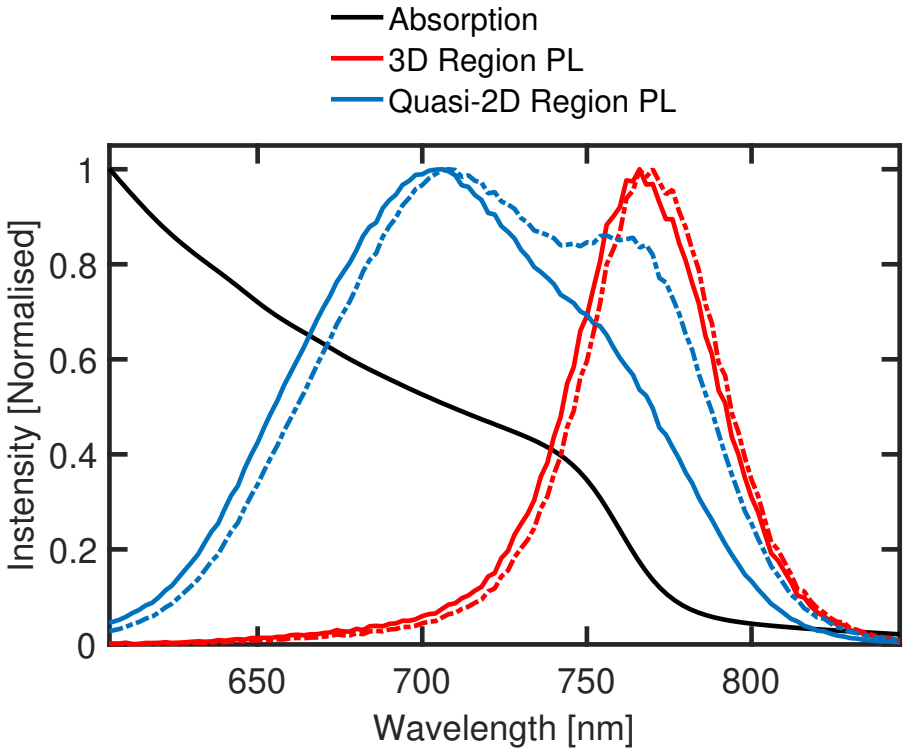

Figure S12: The PL spectrum measured for front and back excitation of the mixed quasi-2D/3D perovskite film, shown with the normalised absorption spectrum. Dashed lines show the uncorrected PL spectra data, while solid lines show the PL spectra after correcting for photon reabsorption, as described in the text. Details of how the PL spectra were collected are given in Section 1.4

described above. This produces a matrix which describes how PL emission from each slice in the model results in reabsorption by each other slice. The individual PL spectrum of each region was used, and because of this the PL across the sample is said to be modelled as being 'heterogeneous' PL.

5 Fits to THz Photoconductivity Data

This section shows the fits of the dynamical model described in Section 4.2 to the THz photoconductivity transients measured for the mixed quasi-2D/3D perovskite film. The fits are shown with the data, first, for the case of excitation from the front side of the perovskite film, and also for the case of excitation from the back side.

Before describing the fits, the four different dynamical models used to fit the THz photoconductivity decays, are first described and the parameters used in the fitting process are explained.

Parameters Used in Dynamical Model For excitation from each side of the mixed quasi-2D/3D perovskite film, four different simulations of the charge-carrier dynamics were globally fitted against the experimental THz photoconductivity transients. Each simulation uses the self-absorption model from Section 4.2, but across the different simulations charge-carrier diffusion and photon reabsorption are included or excluded from the model, as indicated in Figures S13 and S14. This highlights how diffusion and photon reabsorption individually contribute to the charge-carrier dynamics.

The maximum pump-excitation fluence used was $16\,\mu J\,cm^{-2}$. This was sufficiently low that any Auger-like recombination processes were not considered in the fitting, with k_3 being fixed at zero. Additionally, monomolecular decay is not considered and k_1 is fixed at zero. This is because the PL lifetime of the mixed quasi-2D/3D perovskite film (in the range 750 nm–800 nm) was determined to be $\approx$1 µs (Section 2), while the maximum time delay in the THz photoconductivity experiment was 1.2 ns. Since the monomolecular lifetime far exceeds the experimental time window, mono-molecular decay will not be observed. This means the only free parameter in the model was k_2, as Auger and monomolecular recombination are not considered.

Excitation from the front and back sides of the mixed quasi-2D/3D perovskite film were considered separately. In each case, k_2 was globally fitted across a set THz photoconductivity

transients measured for a range of pump-excitation fluences. The fitting routine also made small adjustments to the values of the pump powers used in the dynamical model, to allow the model to fit the experimental data. This accounts for small errors in the measurement of the pump beam power.

Excitation from the Front of the Perovskite Sample Figure S13 shows the measured THz photoconductivity transients, for excitation from the front side of the mixed quasi-2D/3D perovskite film, together with the fitted simulations. The separate panels, (a), (b), (c) and (d) in Figure S13 show the same THz photoconductivity decays, fitted with four different dynamical models as described above and as indicated in the figure. As each model either includes or omits charge-carrier diffusion and photon reabsorption, the individual effects of each transport process on the shape of the modelled THz photoconductivity transients can be seen.

The THz photoconductivity transients, measured for excitation of the front side of the mixed quasi-2D/3D perovskite film, show a simple decay of THz photoconductivity over time. The rate of this decay increases as the excitation fluence increases, consistent with there being more bimolecular recombination at higher charge-carrier densities. All of the simulations can fit the THz photoconductivity decays well, however, each fits the same curve using a different value for the bimolecular recombination rate, k_2. This reflects that although the models all fit the data, they make different assumptions about the charge-carrier dynamics. It can also be seen that the faster initial decay within the first 100 ps is fitted more closely only by the models which include charge-carrier diffusion.

Excitation from the Back of the Perovskite Sample The THz photoconductivity transients, for excitation from the back side of the mixed quasi-2D/3D perovskite film, are shown in Figure S14. As before, the THz photoconductivity transients in each panel of Figure S14 show the same data, but in each case a different dynamical model is used.

Unusually, Figure S14 shows that several of the THz photoconductivity transients rise,

rather than decay, within the first 500 ps. After this initial rise the THz photoconductivity transients decay, in the same manner as the THz photoconductivity transients for front-side excitation. Once again the THz photoconductivity transients for higher excitation fluences decay faster than those where the excitation fluence was lower.

By comparing panels (a) – (d) in Figure S14 it can be seen that charge-carrier diffusion must be included in the dynamical model to simulate the experimentally observed rise in THz photoconductivity. The top row of Figure S14 shows the two simulations which do not include charge-carrier diffusion (where one model includes and the other omits photon reabsorption). It can be seen that none of the transients produced by these dynamical models show any rise in THz photoconductivity. In contrast, the bottom two simulations in Figure S14 both include charge-carrier diffusion and each set of simulated transients reproduce the rise in THz photoconductivity seen in the experimental data.

The exact shape of the transients and the role of each of the transport processes is fully discussed in Section 6, but from Figure S14 it is already clear that diffusion is chiefly responsible for the rise in THz photoconductivity seen on the quasi-2D side of the mixed quasi-2D/3D perovskite film.

***

The values of bimolecular recombination rate constant k_2 obtained for the mixed quasi-2D/3D perovskite film are, $k_2 = 7.1 \times 10^{-10}\,\mathrm{cm^3\,s^{-1}}$ for excitation from the front side and $k_2 = 6.7 \times 10^{-10}\,\mathrm{cm^3\,s^{-1}}$ for excitation from the back side. We note that the average of these two values ($6.9 \times 10^{-10}\,\mathrm{cm^3\,s^{-1}}$) is remarkably close to the previously published[S3] value of $k_2 = 6.8 \times 10^{-10}\,\mathrm{cm^3\,s^{-1}}$ for a conventional $MAPbI_3$ film. The fact that the same bimolecular recombination rate can describe the charge-carrier dynamics in both the mixed quasi-2D/3D perovskite film and a regular $MAPbI_3$ film, highlights the intrinsic nature of bimolecular recombination in lead-halide perovskites. For the rest of the modelling work undertaken around the mixed quasi-2D/3D perovskite film, this average value of $k_2 = 6.9 \times 10^{-10}\,\mathrm{cm^3\,s^{-1}}$ is used as the bimolecular recombination rate constant throughout the entire perovskite film.

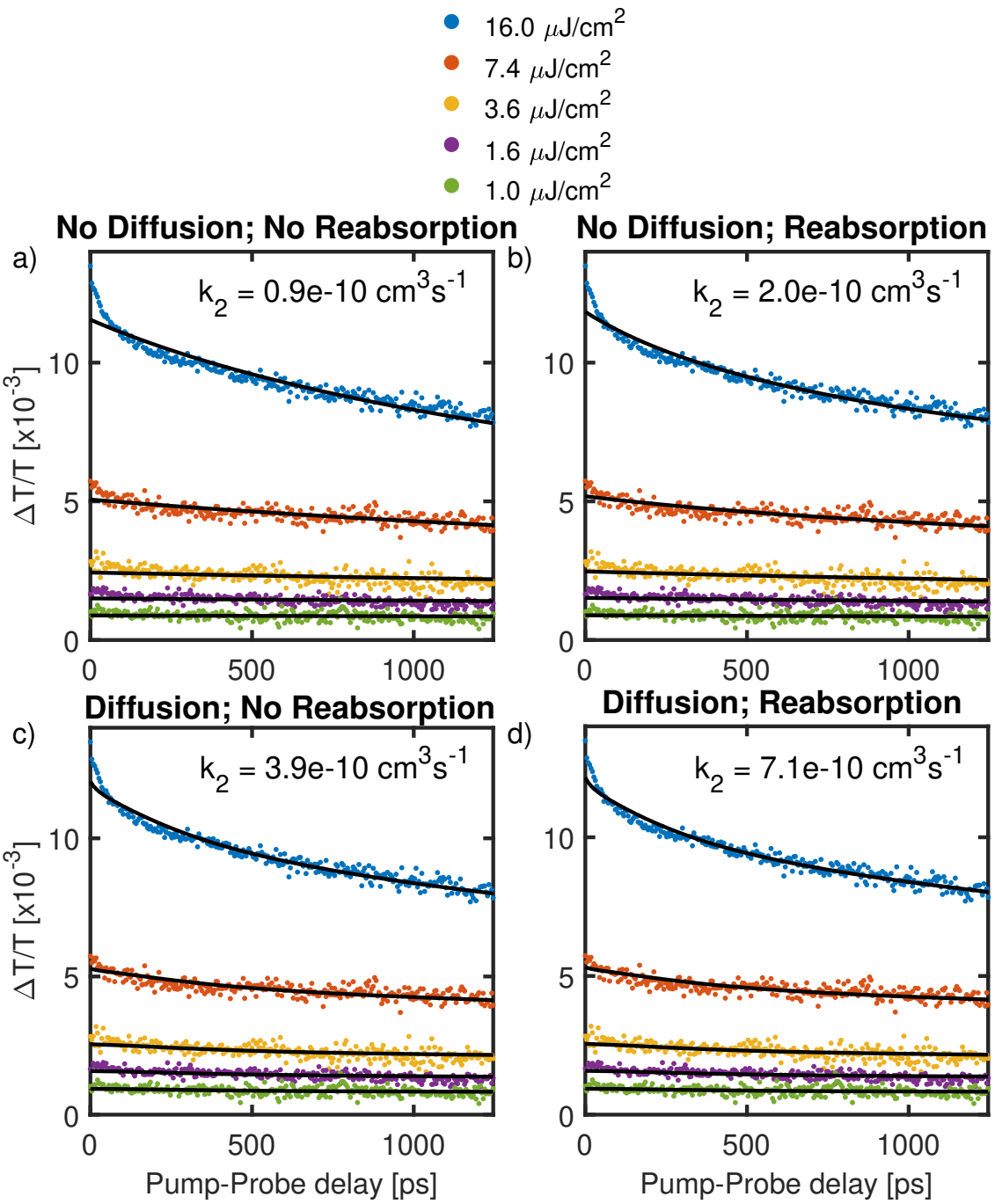

Figure S13: THz photoconductivity transients measured for excitation from the front side of the mixed quasi-2D/3D perovskite film with a pump wavelength of 400 nm, shown with global fits based on the self-absorption model (black lines). In each panel, charge-carrier diffusion and photon reabsorption are either included or omitted from the dynamical model, as indicated.

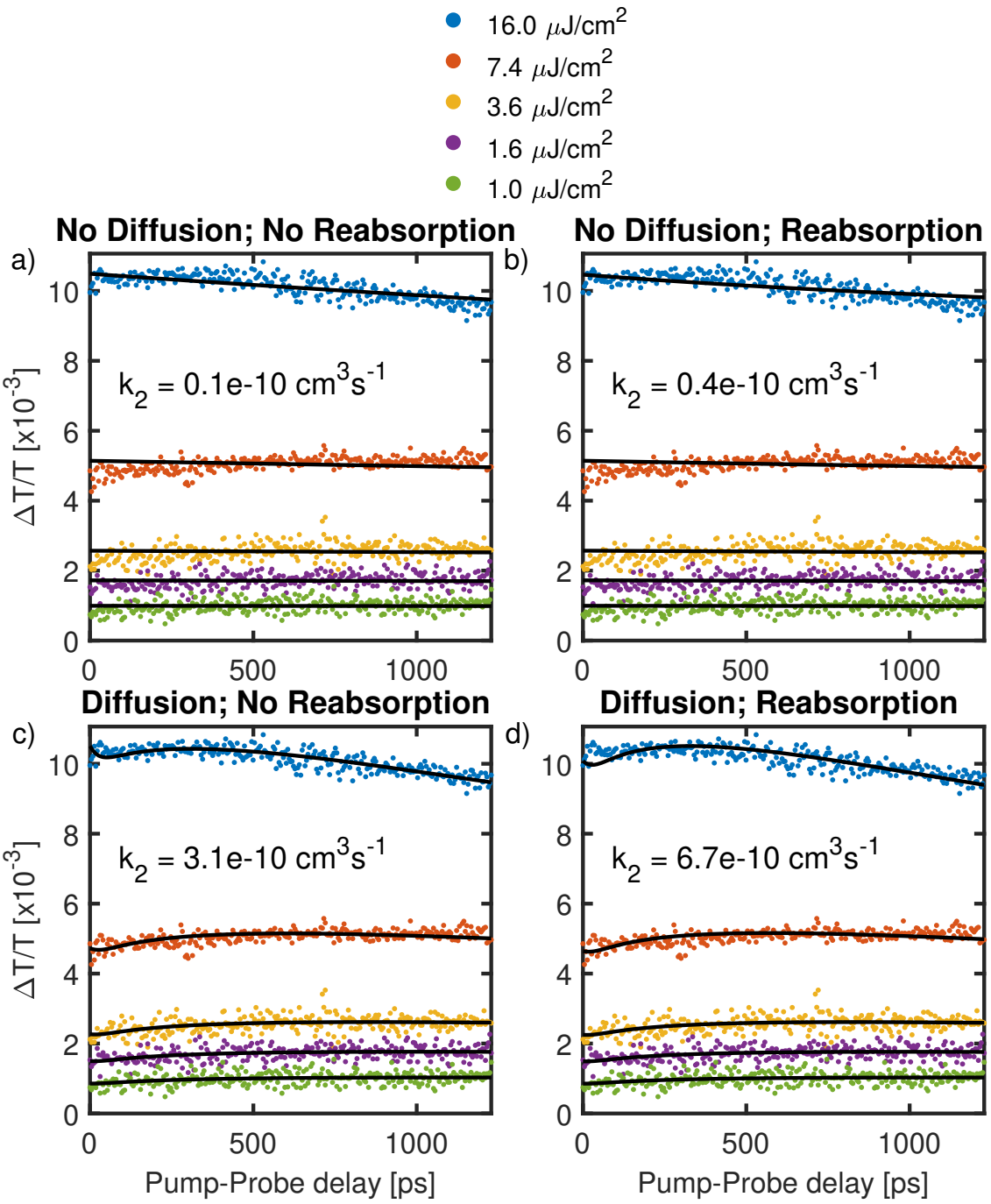

Figure S14: THz Photoconductivity transients measured for excitation from the back side of the mixed quasi-2D/3D perovskite film with a pump wavelength of 400 nm, shown with global fits based on the self-absorption model (black lines). In each panel, charge-carrier diffusion and photon reabsorption are either included or omitted from the dynamical model, as indicated.

6 Analysis of the Shape of the THz Photoconductivity Transients

In this section the influence of charge-carrier diffusion, photon reabsorption and the thickness of the quasi-2D region on the shape of the THz photoconductivity transients will be discussed. Considering each of these factors in turn allows a fuller understanding of the charge-carrier dynamics in the mixed quasi-2D/3D perovskite film. The reason for the rise in THz photoconductivity, when the sample is excited from the back, will be explained. The role of photon reabsorption, and in particular the impact of the blue-shifted PL spectrum of the quasi-2D region will also be presented. Finally the impact of the thickness of the quasi-2D region upon the speed and shape of the rise in THz photoconductivity is demonstrated.

In each of the following subsections reflection losses of the optical pump pulse, as it enters the sample, are not considered. This allows the charge-carrier dynamics for back and front side excitation to be analysed under identical pump-excitation, without any in-coupling effects. Internal reflections of emitted PL are still considered as part of the ray tracing model.

All simulations use the simplified model of the mixed quasi-2D/3D perovskite film, developed in Section 4.1 and based on sample profilometry data and the STEM image in Figure 1a) of the main manuscript. This assumes the perovskite film is separated into a quasi-2D region of 150 nm and a 3D region of 300 nm, with total thickness 450nm. The properties of both regions are identical, except for their PL emission spectra and their charge-carrier mobilities. Additionally, all simulations nominally assume $k_2 = 6.9 \times 10^{-10}\,\mathrm{cm^3\,s^{-1}}$ across both regions of the modelled film.

6.1 Impact of Charge-Carrier Diffusion

Although the rise in THz photoconductivity has already been attributed to charge-carrier diffusion in Section 5, the mechanism behind this rise will now be discussed. The basis of this discussion will be a set of simulated THz photoconductivity transients, which include

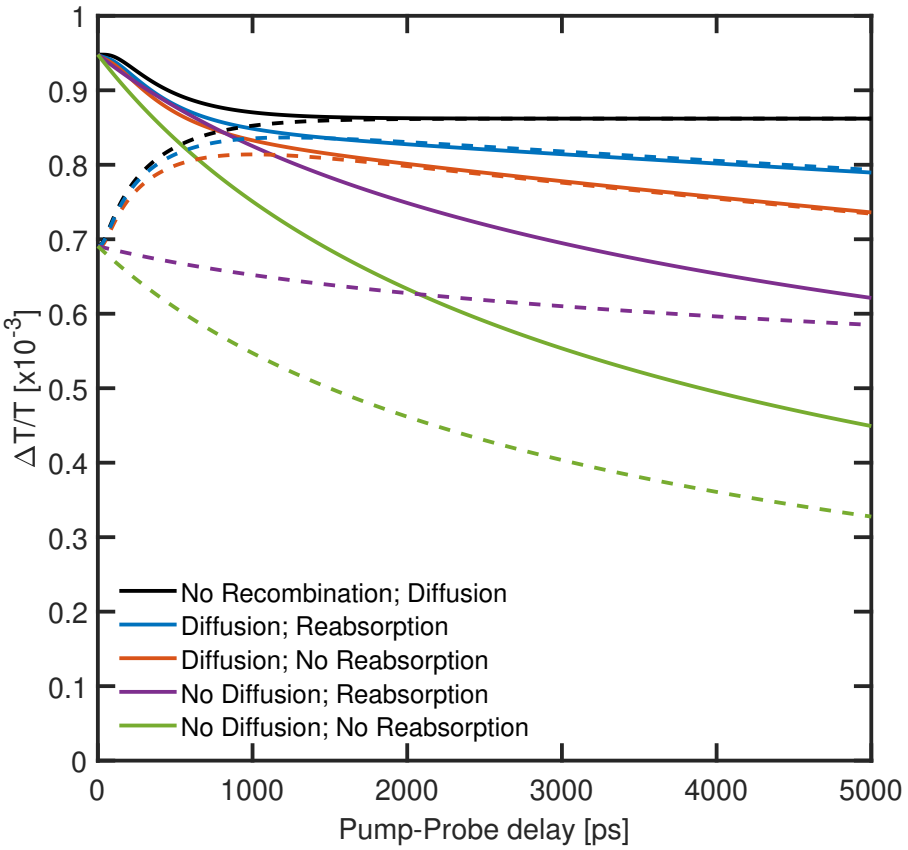

Figure S15: Simulated THz photoconductivity transients for the mixed quasi-2D/3D perovskite film, showing the effect of including different combinations of charge-carrier diffusion, photon reabsorption, and recombination in the dynamical model. Solid lines indicate the perovskite film is excited from the front side, while dotted lines indicate excitation from the back side. All simulations are modelled using an incident fluence of $1.0\,\mu J\,cm^{-2}$ and with $k_2 = 6.9 \times 10^{-10}\,cm^3\,s^{-1}$. Reabsorption simulations use heterogeneous PL as described in Section 4.1.

different combinations of charge transport processes. This approach allows the individual effects of charge-carrier diffusion, photon reabsorption and charge-carrier recombination to be understood in isolation from each other. To understand charge-carrier diffusion, the discussion here will focus on the simulations involving charge-carrier diffusion, with and without charge-carrier recombination.

Under Which Circumstances Is There a Rise in THz Photoconductivity? Figure S15 shows simulated THz photoconductivity transients for the lowest excitation fluence utilised in OPTP spectroscopy ($1.0\,\mu J\,cm^{-2}$). The simulations use the same model parameters, but different combinations of charge transport processes are included in each. The blue, orange and black curves in Figure S15 represent simulations that all include charge-carrier diffusion and it can be seen that in these cases a rise in THz photoconductivity is seen, when the perovskite film is excited from the back side. Conversely, in the simulations represented by the purple and green curves, which do not account for charge-carrier diffusion, no initial rise in THz photoconductivity can be seen. This is consistent with the dynamical models presented in Section 5, where no rise in the simulated THz photoconductivity was seen, except where diffusion was included. Therefore, the rise in THz photoconductivity appears only in simulations where charge-carrier diffusion is accounted for. Additionally, since this rise is seen in the experimental THz photoconductivity transients, it is clear that diffusion plays some role in the charge-carrier dynamics.

The Cause of the THz Photoconductivity Rise. By considering the charge-carrier dynamics in the absence of recombination, the mechanism behind the THz photoconductivity rise can be more clearly understood. Figure S16 shows a simulated THz photoconductivity transient, for excitation from the back side of the sample. The THz photoconductivity is simulated accounting for charge-carrier diffusion, but assuming no recombination (identical to the dotted black line in Figure S15). In this case, along with the simulated THz photoconductivity, the fraction of charge carriers present in each region of the film is also shown.

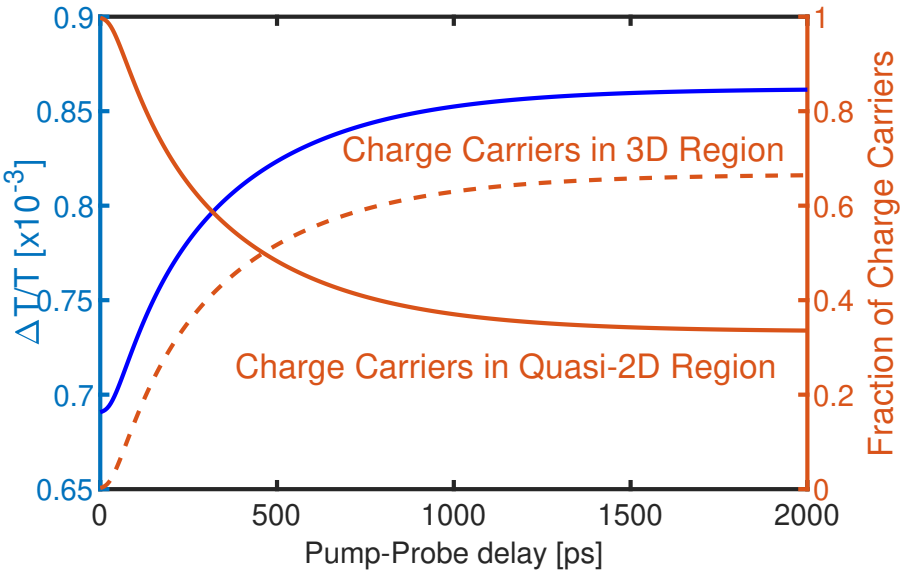

Figure S16: Simulated THz photoconductivity transient for excitation from the back of the mixed quasi-2D/3D perovskite film, at an excitation fluence of 1.0 µJ cm^{-2}, modelled assuming charge-carrier diffusion and no recombination.. Shown with the fraction of charge carriers present in each region of the model. It can be seen that the increase in THz photoconductivity correlates exactly with the number of charge carriers in the 3D region.

It can be seen that, in parallel with the rise in THz photoconductivity, there is an identical rise in the number of charge carriers which have diffused into the 3D region of the sample. This clearly indicates that diffusion of charge carriers out of the quasi-2D region and into the 3D region is the source of the rise in THz photoconductivity.

The reason that diffusion of charge carriers between the quasi-2D and 3D regions produces a change in THz photoconductivity is that the charge-carrier mobility of the quasi-2D region is lower than that of the 3D region. In an OPTP experiment, the THz photoconductivity produced by a sample is proportional to both the number and mobility of the charge carriers[S5]. For the mixed quasi-2D/3D perovskite film, the charge-carrier mobility of the quasi-2D region is less than that of the 3D region. This means that, charge carriers in the quasi-2D region produce a smaller THz photoconductivity signal than those in the 3D region. Movement of charge carriers between the two regions, therefore, results in a change in the total THz photoconductivity.

The case where the mixed quasi-2D/3D perovskite film is excited from the back is il-

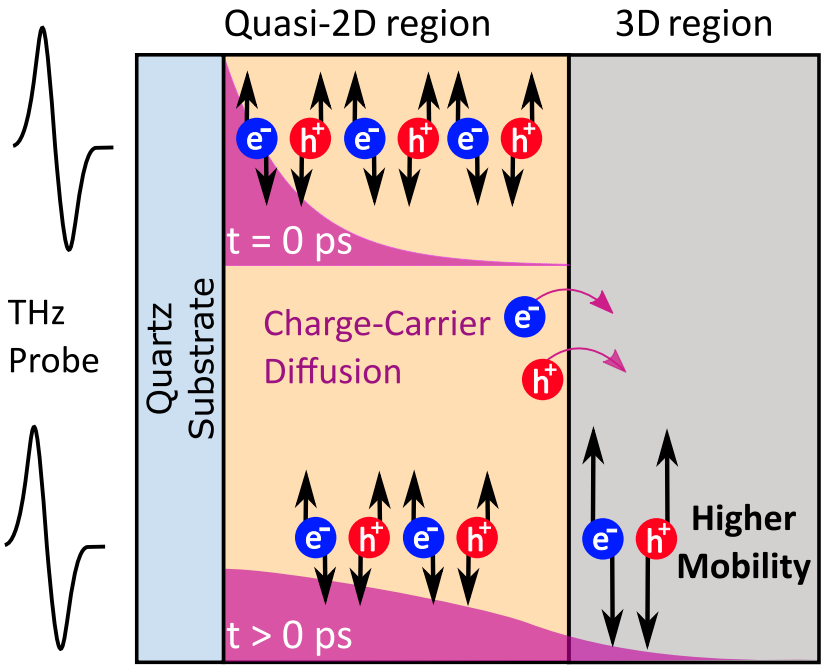

Figure S17: Illustration showing how the movement of charge carriers, from the lower charge-carrier mobility quasi-2D region into the higher mobility 3D region, causes an increase in the total THz photoconductivity of the mixed quasi-2D/3D perovskite film.

lustrated in Figure S17. Initially, the charge carriers are generated in the quasi-2D region and have a low charge-carrier mobility. However, over time, diffusion causes some of the charge carriers to transfer from the quasi-2D region into the 3D region, raising their mobility. This increase in charge-carrier mobility results in the experimentally measured rise in THz photoconductivity.

Charge-Carrier Diffusion and the Shape of the THz Photoconductivity Transients In the context of the modelled transients in Figure S15, the effects of charge-carrier diffusion can now be explained. When the back side of the sample is excited, the initial rise in THz photoconductivity comes from the increase in charge-carrier mobility as diffusion moves charge carriers from the quasi-2D region into the 3D region. This rise is seen only in the simulations involving diffusion, as otherwise the charge carriers are not transferred into the 3D region. The reasons why photon reabsorption cannot cause a similar rise in THz photoconductivity, are discussed in Section 6.2.2.

For the case where the sample is excited from the front, diffusion of charge carriers causes a drop in THz photoconductivity over the first ns, rather than a rise. This is because charge carriers now diffuse from the 3D region to the quasi-2D region, where their mobility is lower. The drop in charge-carrier mobility adds to any recombination losses and gives an initial fast decrease in THz photoconductivity for simulations including diffusion.

By comparing the simulated THz photoconductivity transients for the simulations which account for charge-carrier diffusion and recombination to those where there is no recombination, it can now be seen that much of the change in THz photoconductivity within the first ns is caused by movement of charge carriers between the two regions, rather than by recombination. Distinguishing between the change in THz photoconductivity caused by charge-carrier diffusion and that caused by recombination is important. Otherwise, the charge-carrier recombination rate (k_2) is overestimated when the sample is excited from the front and underestimated when it is excited from the back.

An additional effect of diffusion on the charge-carrier dynamics is the supression of higher-order recombination processes. At the charge-carrier densities being studied, the principal recombination mechanism is bimolecular recombination, which is proportional to n^2. Initially, as the absorption length of the pump beam is short, the charge carriers are highly concentrated on one side of the perovskite film (depending on the side from which the perovskite was excited). This means that n^2 is large and bimolecular recombination is initially very strong. However, as diffusion spreads the charge carriers out over more of the film, the average n is reduced, and so the rate of bimolecular recombination slows.

Figure S15 shows that when diffusion is omitted from a simulation, charge carriers are lost much faster than when diffusion is included. It can also be seen that the THz photoconductivity transients for back and front excitation rejoin by $\approx 2\,\text{ns}$. This indicates that regardless of which side the perovskite film was excited from, by this time there are now the same number of charge carriers in each region. After the initial charge-carrier distribution has flattened, diffusion plays no further role and the THz photoconductivity transients

continue to decay.

Conclusions. In summary, diffusion shapes the THz photoconductivity transients in two ways. Firstly it has been shown that the initial rise in THz photoconductivity, when the samples are excited from the back, is caused by diffusion. As the charge carriers diffuse from a lower to higher mobility, the THz photoconductivity increases, which produces the observed rise, seen experimentally. Without accounting for diffusion there is no way to simulate such a rise in THz photoconductivity. Secondly diffusion also lowers the charge-carrier density, which reduces the amount of bimolecular charge-carrier recombination in the sample.

Accounting for the movement of charge carriers between regions of different charge-carrier mobility gives a clear physical explanation for the rise in THz photoconductivity measured for the mixed quasi-2D/3D perovskite film. This highlights the importance of including charge-carrier movement when modelling their dynamics, as otherwise the shape of the THz photoconductivity transients cannot be understood. The simulations have also shown that, despite the sharp fall in THz photoconductivity when exciting from the front, charge carriers are not being lost, but are still present with a reduced mobility. As the charge carriers have not recombined they could potentially still be extracted. Based on this interpretation of the charge-carrier dynamics, it can be seen that the rise in THz photoconductivity provides evidence of charge-carrier transfer from the quasi-2D to the 3D region.

6.2 Impact of Photon-Reabsorption

Photon-reabsorption refers to a semiconductor's absorption of its own emitted photons, exciting new charge carriers. This process is important in normal 3D perovskite films,[S6,S7] as it reduces the number of charge carriers lost through radiative recombination. In the mixed quasi-2D/3D perovskite film photon reabsorption is particularly important as the quasi-2D region emits PL above the bandgap of the 3D phase, meaning it will be strongly reabsorbed.

In this section the role of photon reabsorption in the charge-carrier dynamics of the mixed

quasi-2D/3D perovskite film is considered. It will be shown that photon reabsorption slows the rate of charge-carrier recombination throughout the entire film. However, it will also be shown that the blue-shifted PL emitted from the quasi-2D region is reabsorbed more strongly than the PL emitted from the 3D region. At the end of the section, an analytical expression will be derived showing the conditions under which photon reabsorption could give a rise in THz photoconductivity.

6.2.1 Influence of Photon-Reabsorption on Charge-Carrier Dynamics

In discussing photon reabsorption, the most important factor is how strongly a perovskite film absorbs light at the wavelength where PL is emitted. Stronger absorption will lead to a higher fraction of the emitted photons being recaptured. This excites new charge carriers, effectively slowing the rate of radiative recombination in the perovskite film.

The novel aspect of the mixed quasi-2D/3D perovskite film is that it is composed of two different regions, which are modelled as having two different PL spectra. Although the quasi-2D and 3D regions are simulated as having separate PL spectra, because the 3D phase absorption profile is dominant in Figure S1, this absorption spectrum is taken to apply throughout the perovskite film. This is important, as it means the quasi-2D PL, which is blue-shifted by quantum confinement, is much more strongly reabsorbed than PL emitted by the 3D region.

Here, the effects of photon reabsorption on the charge-carrier dynamics of the mixed quasi-2D/3D perovskite film will be discussed, as two separate points. First, the role of photon reabsorption in slowing the charge-carrier recombination, across the entire perovskite film, is addressed. Secondly, the effect of the enhanced photon reabsorption of the PL emitted from the quasi-2D region is discussed.

As in the analysis of charge-carrier diffusion in Section 6.1, the discussion will rely on a set of simulated THz photoconductivity transients, shown in Figure S18. The THz photoconductivity transients are simulated for back and front side excitation of the mixed quasi-2D/3D

perovskite film, in all cases using the same excitation fluence. Across the different simulations, charge-carrier diffusion, recombination and photon reabsorption are either included in, or omitted from, the dynamical model. This allows the effect of photon reabsorption on the shape of the THz photoconductivity transients to be separated from the effects of charge-carrier diffusion and recombination.

The details of the ray-tracing model used to simulate photon reabsorption are discussed in Section 4.3. Unless otherwise specified, the quasi-2D and 3D regions are modelled as having separate PL spectra, termed 'Heterogeneous PL', as described in Section 4.1.

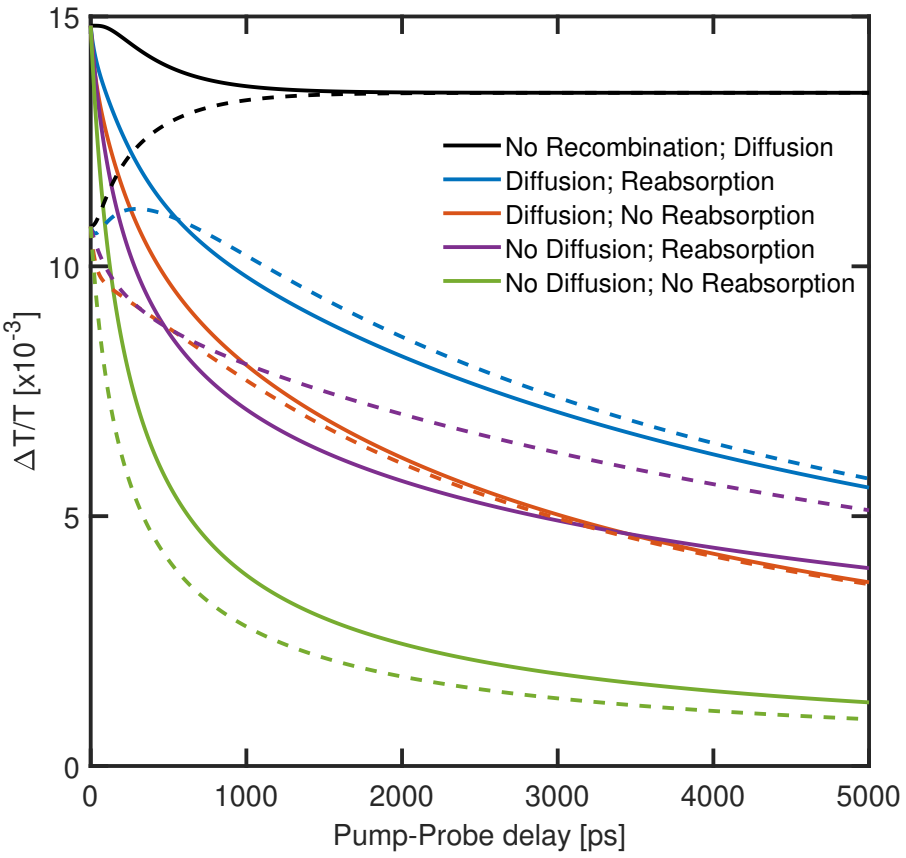

Figure S18: Simulated THz photoconductivity transients for the mixed quasi-2D/3D perovskite film, showing the effect of including different combinations of charge-carrier diffusion, photon reabsorption, and recombination in the dynamical model. Solid lines indicate the perovskite film is excited from the front side, while dotted lines indicate excitation from the back side. All simulations are modelled using an incident fluence of $16\,\mu J\,cm^{-2}$ and with $k_2 = 6.9 \times 10^{-10}\,cm^3\,s^{-1}$. Reabsorption simulations use heterogeneous PL as described in Section 4.1.

Effect one: Reduction in Bimolecular Recombination Losses. The first trend which can be established from Figure S18 is that photon reabsorption slows down charge-carrier decay. This trend can be seen in the solid lines shown in Figure S18, which are the THz photoconductivity transients for the case where the front side of the sample is excited. It can be seen that compared to the simulation where neither charge-carrier diffusion nor photon reabsorption is accounted for (green lines), adding photon reabsorption to the model (purple lines) drastically slows the decay of THz photoconductivity. The explanation for this is that just as many charge carriers decay as before, however, photon reabsorption causes some of the photons emitted by bimolecular recombination to be recovered again as charge carriers. The suppression of bimolecular recombination by photon reabsorption in a similar fashion has been seen before in MAPI and GaAs[S3,S8].

When charge-carrier diffusion is also accounted for, the same slowing down of THz photoconductivity decay is observed, as can be seen from the orange and blue lines in Figure S18. Both simulations account for charge-carrier diffusion, but since the blue line also includes photon reabsorption, it shows a much slower THz photoconductivity decay than the orange line.

Figure S18 shows that charge-carrier diffusion and photon reabsorption both act to reduce the decay of charge carriers in the mixed quasi-2D/3D perovskite film. Although charge-carrier diffusion alone can produce the experimentally observed rise in THz photoconductivity, both charge-carrier diffusion and photon reabsorption act to reduce charge-carrier decay and so it is important to consider both processes. Unless photon reabsorption is included in the dynamical model, it will wrongly be concluded that bimolecular recombination is slower than it really is and k_2 will be underestimated[S3].

Effect Two: Slower Charge-Carrier Recombination in the Quasi-2D Region. The second and more subtle effect of photon reabsorption is that it causes more charge carriers to be retained if they are excited into the quasi-2D region rather than the 3D region. This effect

can be seen in Figure S18, where the the dotted lines show THz photoconductivity transients when the back of the sample is excited, while solid lines show front excitation. Although the lower charge-carrier mobility of the quasi-2D region means the THz photoconductivity will initially be lower when the back side of the sample is excited, diffusion of charge carriers should mean that the two lines eventually meet as the charge carriers spread evenly across the sample. However, Figure S18 shows that where photon reabsorption is present, the lines cross over and the THz photoconductivity at the end of the simulation is higher for back excitation than front excitation. As the THz photoconductivity is higher when the mixed quasi-2D/3D perovskite film is excited from the back, even after the charge carriers have diffused across the sample, this means that the charge carriers must decay more slowly in the quasi-2D region.

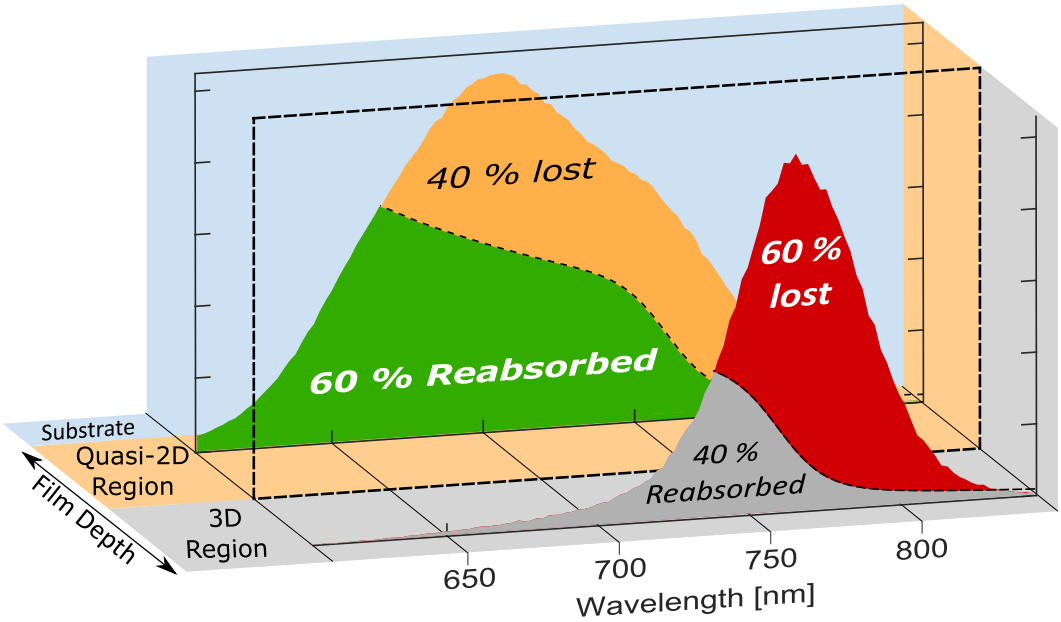

Figure S19: An illustration of how the PL emitted from the quasi-2D region is absorbed more strongly by the mixed quasi-2D/3D perovskite film than the PL emitted from the 3D region. PL spectra are taken from Figure S12 and reabsorption probabilites are taken from Figure S20.

The model has shown that in the quasi-2D region, charge carriers decay more slowly overall; now the mechanism for this slower recombination will be investigated. As the quasi-2D region in the model differs from the 3D region only in charge-carrier mobility and PL

spectrum, the higher charge-carrier retention for back-side excitation must arise from one or both of these two features. However, the lower mobility of charge carriers in the quasi-2D region will slow down charge-carrier diffusion, resulting in higher charge-carrier densities being present for longer times. If this was the only difference between the two regions, it would therefore, result in faster bimolecular recombination when the sample is excited from the back, which is the opposite of what is observed experimentally. This rules out the difference in charge-carrier mobility between the two regions being the cause of the slower charge-carrier recombination in the quasi-2D region.

On the other hand, although having a different PL spectrum will not impact the number of charges recombining, it will cause a difference in how they are reabsorbed. As the quasi-2D PL spectrum is blue-shifted compared to the absorption onset of the 3D phase, the sample will absorb the emission from the quasi-2D region much more strongly than that of the 3D region PL, as shown in Figure S19. The protective effect which reduces charge-carrier losses in the quasi-2D region can therefore be attributed to enhanced photon reabsorption of the quasi-2D PL, rather than a charge diffusion effect.

Having identified that the difference in the PL spectrum between the quasi-2D and 3D regions impacts the charge-carrier dynamics, it is helpful to look in detail at what happens to PL emitted from both regions. Figure S20 shows what happens to PL which is emitted from each point in the model, as calculated by the ray-tracing model described in Section 4.3. The potential fates of an emitted photon are that it will either be absorbed in one of the quasi-2D or 3D regions, or else escape from the perovskite film – by being out-coupled from the sample or lost to scattering processes.

It can be seen that although at least 60% of the light emitted from the quasi-2D region is recaptured by the sample, this number is only 40% for emission from the 3D region. This reflects the higher absorption coefficient of the sample at the quasi-2D PL wavelengths, whereas much of the 3D PL is emitted below the bandgap of the material and so not reabsorbed (see Figure S12). As the probability of recapturing a photon emitted from the

quasi-2D region is higher, this will mean that over time there will be more charges remaining if the back of the sample is excited, compared with the front.

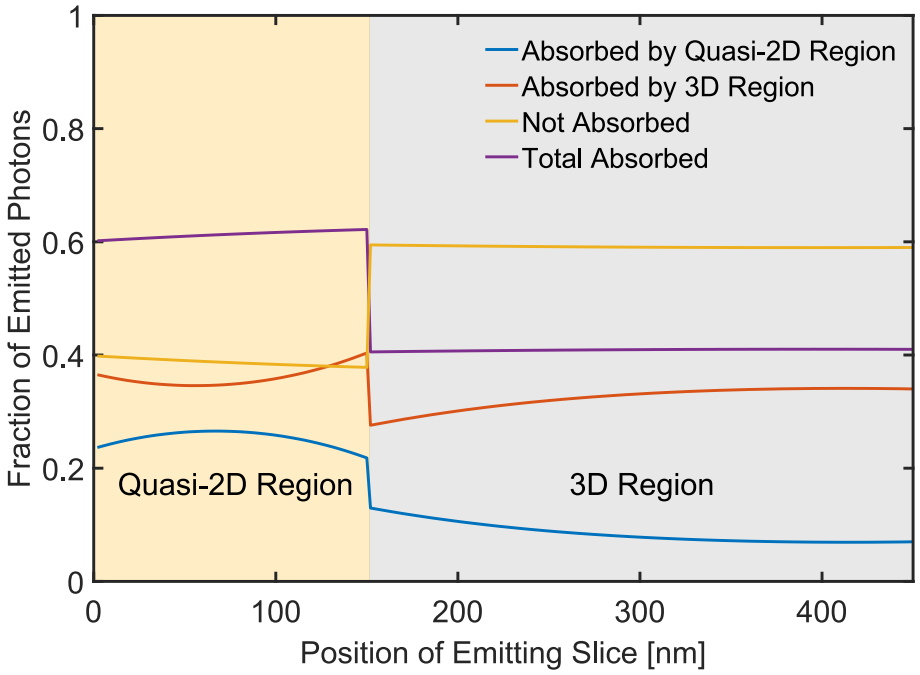

Figure S20: The probability of recapturing an emitted photon, calculated using the ray-tracing model in Section 4.3, shown as a function of the position of the emitting slice from the substrate. Due to the higher-energy PL spectrum, the probability of photon reabsorption is higher for PL emitted from the quasi-2D region.

.

A further demonstration of how the heterogeneous nature of the sample PL causes slower THz photoconductivity decay can be made by modelling the quasi-2D region as having the same PL spectrum as the 3D region. Figure S21 shows THz photoconductivity transients from two simulations, identical except for the simulated PL spectrum used in the quasi-2D region. The 'homogeneous PL' simulation uses the spectrum associated with the 3D phase to model the PL spectrum in both regions of the modelled film. The 'Heterogeneous' case uses the blue shifted PL spectrum, associated with the quasi-2D phase, as the PL spectrum emitted from the quasi-2D region (as described in Section 4.1). It can be seen that when the PL is homogeneous across the perovskite film, the two THz photoconductivity transients meet and no advantage is conferred by the presence of the quasi-2D region. Only when the PL is heterogeneous does exciting the back of the sample cause more charge carriers to be

retained and the THz photoconductivity transients to cross. This confirms that the crossing of the THz photoconductivity is only caused by the PL spectrum in the quasi-2D region being different.

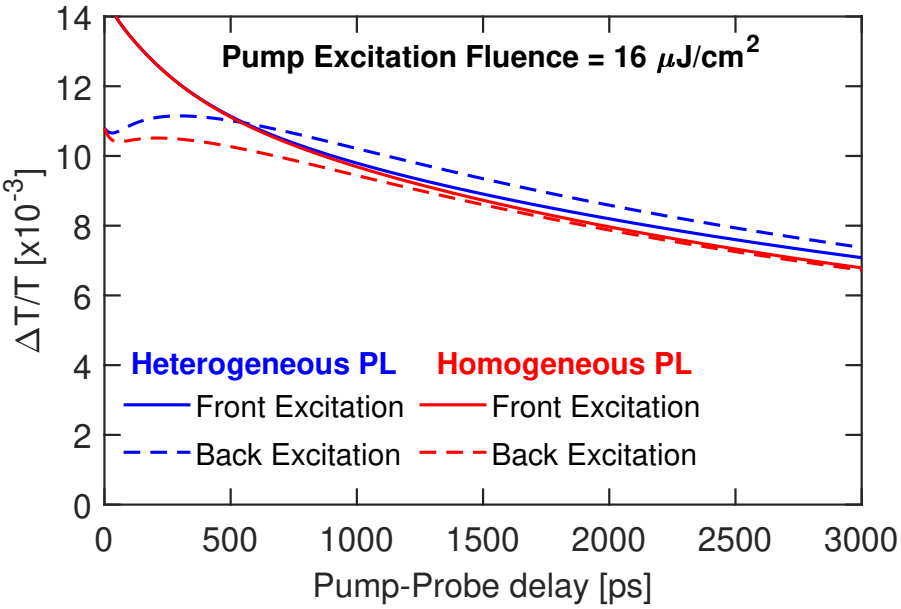

Figure S21: Modelled THz photoconductivity transients demonstrating the boost in photon reabsorption caused by the blue-shift of the quasi-2D PL, using $k_2 = 6.9 \times 10^{-10}\,\mathrm{cm^3\,s^{-1}}$. Heterogeneous PL indicates the quasi-2D region and 3D region are modelled with different PL spectra, as described in Section 4.1, Homogeneous PL indicates that the spectrum associated with the 3D-phase perovskite is used throughout the whole sample.

Conclusions. In summary, it has been shown that the unique composition of the quasi-2D region allows enhanced levels of photon reabsorption. This is because the inclusion of both 2D and 3D domains allows the PL emission to be significantly blue-shifted from the absorption edge and so more strongly recaptured. This enhanced recapture of the quasi-2D PL is especially important, as it has been reported elsewhere[S4] that some 2D perovskites can show increased luminosity, compared with 3D perovskites. However, the enhanced reabsorption of the mixed quasi-2D/3D perovskite film will go some way to offsetting these increased radiative losses, as the surrounding 3D region can efficiently absorb the PL from the 2D material. This more efficient recapture of emitted quasi-2D PL by the surrounding 3D material when the two are mixed together is a useful symbiosis, as it allows the structural

stability of the 2D material to be taken advantage of without losing charge carriers to the increased bimolecular recombination rate.

6.2.2 Can Photon Reabsorption Cause a Photoconductivity Rise?

It has been previously demonstrated in Section 6.1 that diffusion of charge carriers can cause a rise in THz photoconductivity, now the circumstances under which photon reabsorption may cause such a rise will be discussed.

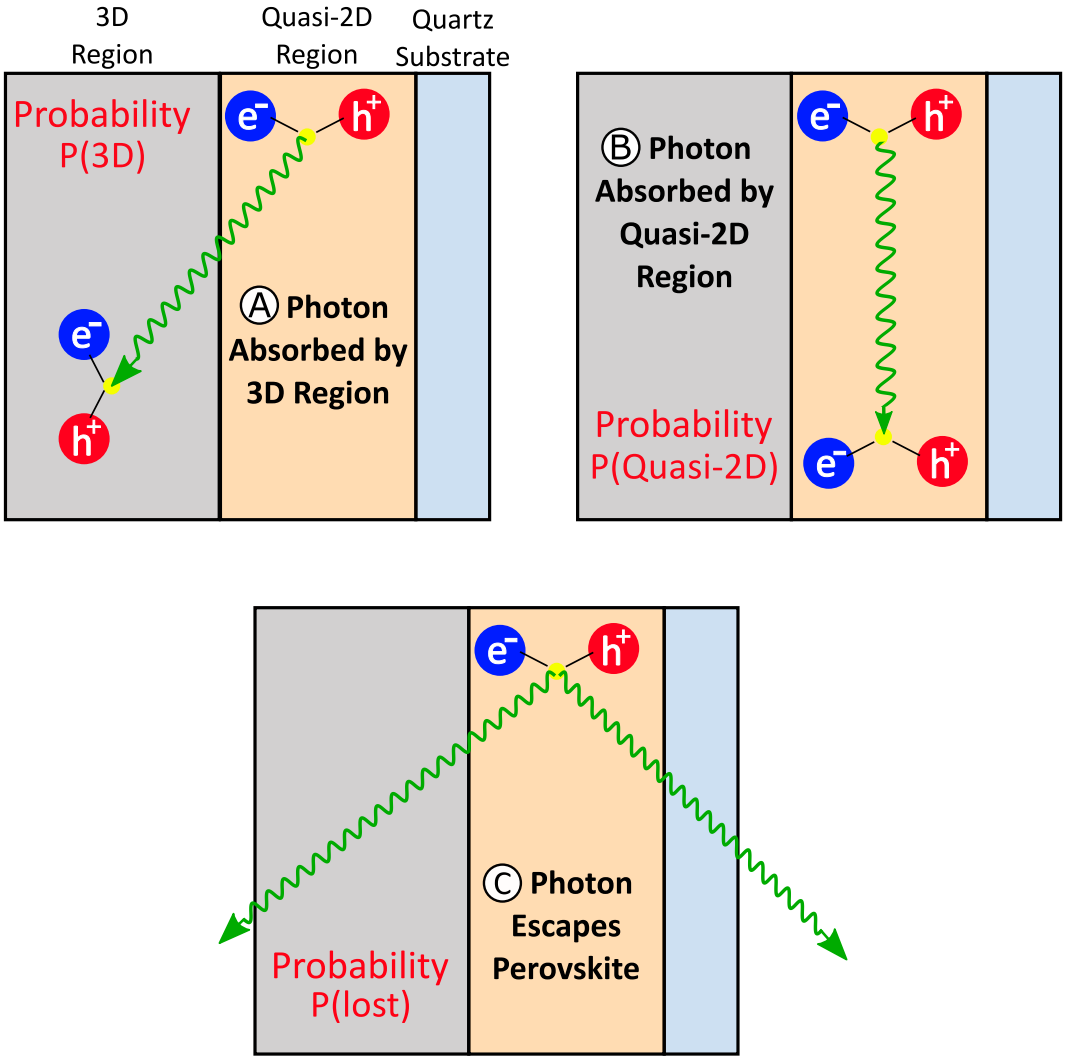

Figure S22: Illustration of the three possible outcomes of PL emission from the quasi-2D region. The emitted photon can be reabsorbed by, (a), the 3D region, or (b), the quasi-2D region. If it is not reabsorbed, the photon is considered lost from the sample as in case (c).

First it is good to summarise why charge-carrier diffusion causes a rise in THz photo-

conductivity. When the mixed quasi-2D/3D perovskite film is excited from the back side, charge carriers are initially generated in the quasi-2D region. Over time, diffusion spreads charge carriers evenly across the film, meaning that some charge carriers are transferred into the 3D region, which has a higher charge-carrier mobility. Since THz photoconductivity is proportional to charge-carrier mobility, it is the transfer of charge carriers from the quasi-2D region into the 3D region which leads to the observed rise in THz photoconductivity.

Since photon reabsorption also transports charge carriers across the sample, it is possible that it could also contribute to the rise in THz photoconductivity, when the sample is excited from the back. For photon reabsorption to cause a rise in THz photoconductivity, charge carriers which decay radiatively in the quasi-2D region must be transferred efficiently into the 3D region, by being reabsorbed there. However, not all of the photons in the quasi-2D region will be reabsorbed in the 3D region.

Figure S22 shows the three possible outcomes of PL emission from the quasi-2D region. Firstly, the emitted photon can be reabsorbed inside the 3D region, with a probability P(3D). Secondly, the photon could be recaptured by the quasi-2D region, with a probability P(quasi-2D). Finally, there is the possibility that the photon is not reabsorbed by any part of the perovskite layer, but is instead lost through scattering or out-coupling. The probability that the photon is lost in this way is given by P(lost). If a charge-carrier is not reabsorbed in either the quasi-2D or 3D regions then it must be lost from the perovskite film. Therefore these three scenarios describe all the possible outcomes of photon emission from the quasi-2D region.

With the possible outcomes of PL emission from the quasi-2D region determined, the next step is to consider how each scenario affects the THz photoconductivity. In the first case, where the emitted photon is recaptured by the 3D region, there will be an increase in THz photoconductivity. This is because one charge-carrier is lost from the quasi-2D region and another is added to the 3D region. The change in THz photoconductivity is proportional to $(\mu_{3D} - \mu_{quasi-2D})$. For the case where the emitted photon is reabsorbed by the quasi-2D

region, the charge-carrier which is lost to recombination is replaced by a charge-carrier with an identical mobility. This means that there is no net change in THz photoconductivity. For the third case, where the photon is lost, there will be a reduction in THz photoconductivity, proportional to $\mu_{quasi-2D}$. This is because a charge-carrier is lost from the quasi-2D region, and not replaced. Therefore, if a charge-carrier is reabsorbed in the 3D region, THz photoconductivity will increase and if it escapes the film, THz photoconductivity will decrease.

The average effect of photon reabsorption across many recombination events can now be calculated. The absorption of charge carriers by the 3D region happens at a probability P(3D), and increases THz photoconductivity $\propto\ (\mu_{3D}-\mu_{quasi-2D})$. The loss of charge carriers by scattering or out-coupling occurs with probability P(lost) and results in a decrease in THz photoconductivity $\propto\ \mu_{quasi-2D}$. If the increase in THz photoconductivity, from transfer into the 3D region, outweighs the loss from charge carriers not being reabsorbed, there will be a net rise in THz photoconductivity caused by photon reabsorption. This criterion can be stated as

$$\mathrm{P(3D)} \times (\mu_{3D} - \mu_{quasi-2D}) > \mathrm{P(lost)} \times \mu_{quasi-2D}. \tag{8}$$

If this equation is satisfied there will be a net rise in THz photoconductivity, caused by photon reabsorption.

In the mixed quasi-2D/3D perovskite film, Figure S20 shows that $P(3D)$ and $P(lost)$ will both be around 0.4. This means there will only be a rise in THz photoconductivity if the difference in charge-carrier mobility between the two regions is greater than the charge-carrier mobility of the quasi-2D region. Since this is not the case, it can, therefore, be concluded that only charge-carrier diffusion will contribute towards a rise in THz photoconductivity in the mixed quasi-2D/3D perovskite film.

In general, Equation 8 shows the relation which must be fulfilled if photon reabsorption is to cause a rise in THz photoconductivity. This happens only in cases where there are extremely low radiative losses, or where the high-mobility phase has a much greater charge-carrier mobility than the low-mobility phase. This can be understood, as, although it

does redistribute charge carriers, photon reabsorption is an intrinsically lossy process, which reduces but does not completely stop the loss of charge carriers.

6.3 Impact of the Thickness of the Quasi-2D Region

The final model parameter which will be examined is the thickness of the quasi-2D region. Both the rise in THz photoconductivity and the crossing of the transients from back and front excitation, rely on differences in the charge-carrier mobility and PL emission spectra between the two sample regions. Therefore, it is instructive to vary the size of the two regions and see how these trends are affected.

In order to investigate how the thickness of the quasi-2D region will impact the charge-carrier dynamics, a series of simulations is used, where the size of the quasi-2D region is varied. In these simulations, the total width of the sample remains constant at 450 nm, so that as the quasi-2D region increases, the 3D region becomes smaller. The results of the simulations are shown in Figure S23, which shows both the modelled THz photoconductivity as well as charge-carrier density. It is helpful to look directly at the charge-carrier density in this case, because as the width of the quasi-2D region decreases, this raises the average charge-carrier mobility of the sample, increasing the THz photoconductivity.

Variation in the Final THz Photoconductivity. From Figure S23, one clear trend is that the final THz photoconductivity decreases as the width of the quasi-2D region increases. This drop in THz photoconductivity can be principally explained by a lower average charge-carrier mobility, rather than faster charge-carrier recombination. Comparing the two parts of Figure S23, the top panel shows a decrease in THz photoconductivity as the thickness of the quasi-2D region increases. Conversely the bottom panel shows an increase in the number of remaining charge carriers. Therefore, as the quasi-2D region grows thicker, there is no dramatic change in charge-carrier recombination. Instead, the reason for the large change in THz photoconductivity can be explained by the lower mobility of charge carriers in the

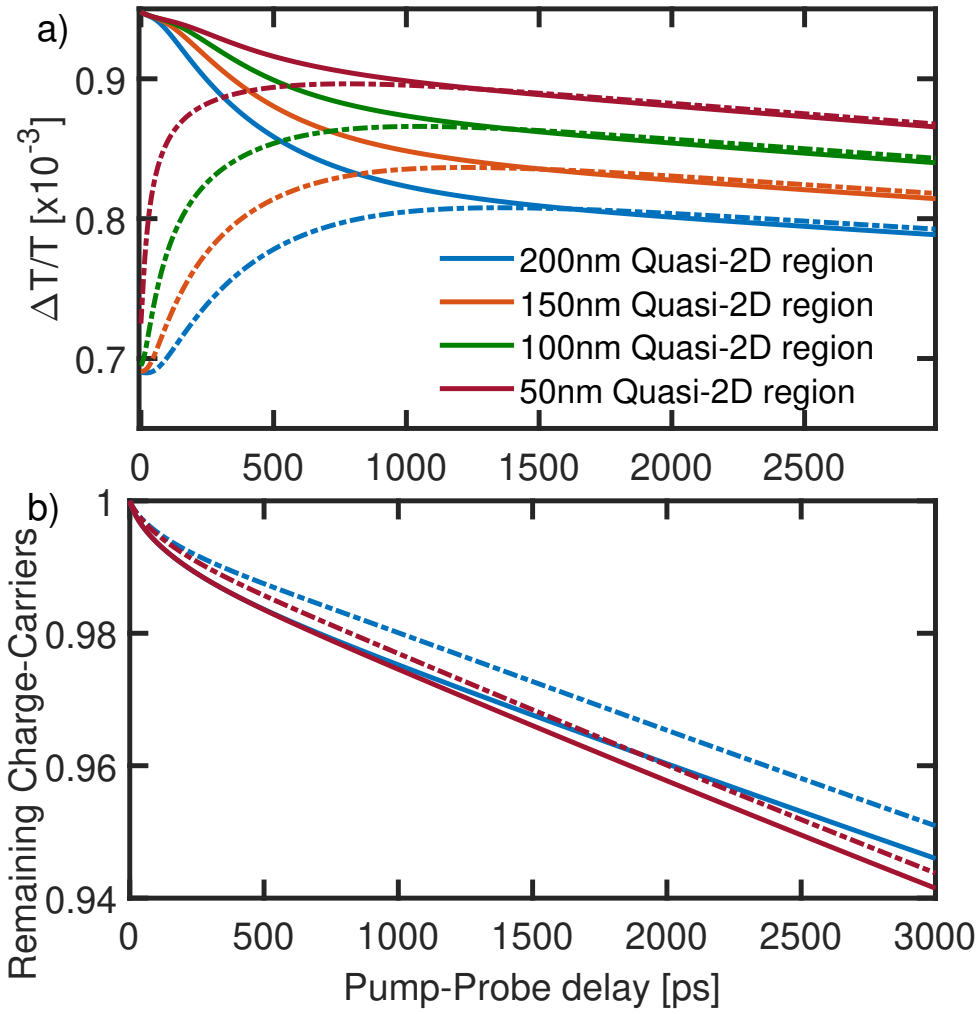

Figure S23: (a) THz photoconductivity transients and (b) charge-carrier density, simulated for mixed 2D/3D perovskite films which have quasi-2D regions of different thickness (the total sample thickness in all cases is 450 nm and the charge-carrier mobilities of the 3D and quasi-2D regions remain $23.9\,\mathrm{cm^2\,V^{-1}\,s^{-1}}$ and $17.4\,\mathrm{cm^2\,V^{-1}\,s^{-1}}$, respectively). Solid lines show excitation from the front side of the perovskite film, while dashed lines show excitation from the back side. The PL spectrum of the sample is Heterogeneous as described in Section 4.3. In each case the excitation fluence used is $1.0\,\mu\mathrm{J\,cm^{-2}}$ and $k_2 = 6.9 \times 10^{-10}\,\mathrm{cm^3\,s^{-1}}$.

quasi-2D region. In the simulation the charge carriers will diffuse evenly across the sample, so that when the quasi-2D region is thicker, it holds more of the charge carriers. This moves the final THz photoconductivity closer to the initial value for back excitation, as more charge carriers are in the low mobility quasi-2D region.

Variation in the THz-Photoconductivity Rise. As the thickness of the quasi-2D region increases, THz photoconductivity transients for back excitation can also be seen to rise more quickly. The THz photoconductivity rise indicates charge carriers diffusing from the quasi-2D region into the 3D region, and increasing in mobility. When the quasi-2D region is thicker, the charge carriers must diffuse further, so take longer to reach the 3D region. This is reflected in the THz photoconductivity transient taking longer to increase as the quasi-2D region becomes thicker. The THz photoconductivity rise can also seen to become less sharp where the width of the quasi-2D region is thicker.

The rise in THz photoconductivity does not only start at earlier times, but is sharper when the quasi-2D region is thinner. The speed of the THz photoconductivity rise reflects the rate at which charge carriers cross between the two regions of the film. This movement of charge carriers into the 3D region is mainly by diffusion, which is faster where the gradient in n is larger. Initially, the gradient in n is large and the charge carriers diffuse quickly through the film. Further into the film, the gradient in n is smaller, so charge-carrier diffusion slows down. When the boundary between the layers is close to the surface, the fast initial spreading out of charge carriers across the film is seen as the sharp rise. However, as the thickness of the quasi-2D region increases, the boundary between the two regions moves deeper into the film. This means that charge-carrier diffusion will have slowed down and the flux of charge carriers into the 3D region is slower, giving a less sharp rise in THz photoconductivity.

The speed and sharpness of the THz photoconductivity rise are linked with charge-carrier diffusion, and can be seen to decrease as the thickness of the quasi-2D region increases.

Variation in Photon Reabsorption. The photon reabsorption related effects are also altered by the width of the quasi-2D region, as this increases the amount of high-energy PL being emitted within the sample. Figure S23 shows that when there is a wider quasi-2D region, although the THz photoconductivity transients for the back and front of the sample take longer to cross, the transient for excitation from the back rises higher above the transient for front side excitation. This indicates that the overall decay of charge carriers is slower, when more of the sample is composed of the quasi-2D material. From Figure S23(b) it can be seen that indeed more charge carriers are retained when the quasi-2D region is thicker. The difference is particularly pronounced when the sample is excited from the back. This trend can be explained as, when more of the sample is composed of the quasi-2D material, more of the PL released will be strongly reabsorbed by the sample.

It has been shown that a larger quasi-2D region will allow more of the PL to be reabsorbed more efficiently. However it would not be valid to extend the quasi-2D region indefinitely to allow more efficient photon reabsorption, as this would invalidate the assumption that the emitted PL is absorbed predominately by the 3D-phase perovskite. Instead, it is beyond the scope of the current model to determine the optimal fraction of quasi-2D material to include.

Impact of the total thickness of the film. Finally, we also investigate the impact of the total perovskite film thickness. The thickness of the perovskite layer in photovoltaic devices usually lies between 300 - 800 nm.[S1,S9,S10] Thicker films are of course desirable for efficient photon absorption, but in the early years of perovskite photovoltaic research, the optimised film thickness was still limited by the charge-carrier diffusion lengths. However, as the quality of the perovskite layers improved over the last years, thicker layers offering additional photon harvesting, in particular near the band edge, have become the new standard.[S11,S12] In order to evaluate if photon reabsorption would have similar effects for different film thickness, the outcoupling efficiencies were simulated for two different cases, where the ratio between the thickness of the 3D and quasi-2D layers is held constant. The first case

was a 450 nm film comprising a 150 nm quasi-2D layer and 300 nm 3D layer, as previously described in the analysis presented so far. The second case was a 300 nm film comprising a 100 nm quasi-2D layer and 200 nm 3D layer. The calculated outcoupling efficiencies of the PL photons for both cases are summarized in Table S1.

Table S1: Simulated outcoupling efficiency for 300 nm and 450 nm mixed-phase 3D/quasi-2D perovskite films.

Total thickness	3D thickness	Quasi-2D thickness	Outcoupled light	Unabsorbed light
300 nm	200 nm	100 nm	14.13%	25.65%
450 nm	300 nm	150 nm	12.32%	26.72%

Despite the reduced path length required for photons emitted within the thinner perovskite film to escape, the simulations show only a 2% increase in outcoupling efficiency from the 300 nm film compared to the 450 nm film. This is due to the fact that the main factor affecting outcoupling remains photon confinement (and the outcoupling angle is unchanged by film thickness).

6.4 Summary

In this section the shapes of the simulated THz photoconductivity transients modelled for the mixed quasi-2D/3D perovskite film have been discussed.

Diffusion between regions of different charge-carrier mobility was shown to be the driving force behind the experimentally observed THz photoconductivity rise. Additionally, by spreading out the charge carriers, diffusion also reduces the charge-carrier density and so acts to reduce bimolecular recombination.

Excitation of the back of the sample was demonstrated to result in more charge carriers being retained, than when the front is excited. This was linked to increased photon reabsorption of the blue-shifted quasi-2D PL, which is efficiently recaptured by the lower bandgap 3D perovskite. This demonstrates a symbiosis of the quasi-2D and 3D materials.

The quasi-2D material provides structural stability and the 3D material strongly reabsorbs the PL emission from the quasi-2D domains.

Finally the thickness of the quasi-2D region was shown to determine the timing, height and sharpness of the rise in THz photoconductivity. A larger quasi-2D region was also predicted by the model to improve photon retention, although this is limited by the necessity of including sufficient 3D perovskite to efficiently recapture emitted PL from the quasi-2D region. It was also demonstrated that the photon reabsorption efficiency is not greatly affected in thinner films, as the outcoupling angle is not affected by the film thickness.

In conclusion, by including charge-carrier diffusion and photon reabsorption in the dynamical model, the charge-carrier dynamics in the mixed quasi-2D/3D perovskite film have been accurately modelled. Both the observed rise in THz photoconductivity, as well as the crossing of the transients for back and front side excitation are reproduced by the dynamical model. The same approach could be used to model other systems which display non-uniform mobilities or PL characteristics. One such candidate system could be a perovskite single-crystal, with a surface region, which has a low charge-carrier mobility, and a higher-mobility bulk region.

7 Accounting for Reflection Losses

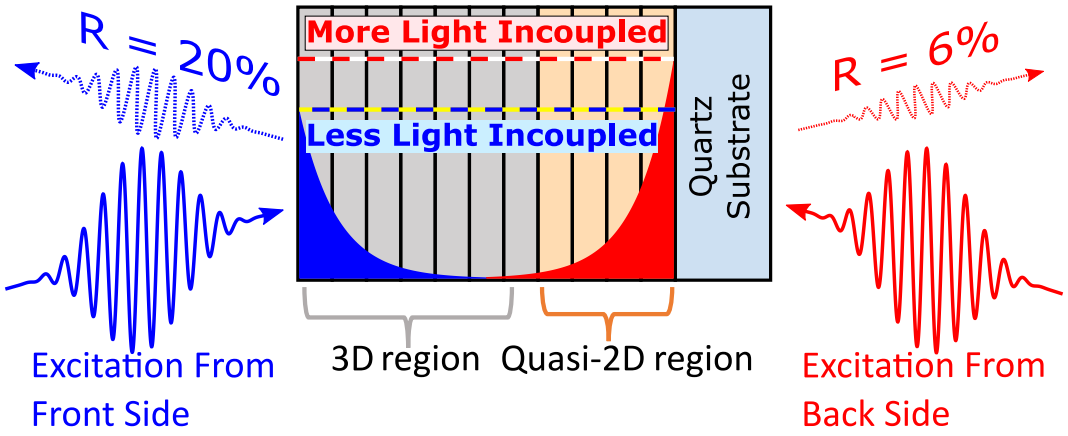

Figure S24: Illustration of how different amounts of the pump beam being reflected by each side of the sample leads to a different number of charge carriers being generated, depending on which side the mixed 2D/3D perovskite film is excited from. The values of the reflection coefficients are taken from FTIR measurements of the mixed quasi-2D/3D perovskite film (Section 1.3).

The modelling work in the previous section represents an idealised situation, where excitation of the mixed quasi-2D/3D perovskite film, from the back or front, results in exactly the same number of charge carriers being generated. This is the ideal way to compare the charge-carrier dynamics for front and back excitation of the perovskite film. However, under real conditions, reflection losses make it difficult to equally excite the front and back of a perovskite film, as illustrated in Figure S24. Using FTIR spectroscopy (see Section 1.3), a reflection loss of 20% was measured for the front side of the mixed quasi-2D/3D perovskite film at 400 nm, but this was only 6% when the excitation is from the front side, due to increased in-coupling through the quartz substrate. This means that the THz photoconductivity transients for excitation of the back and front of the film cannot be directly compared, as different numbers of charge carriers are present in each case.

This section will investigate the extent to which reflection losses influence the comparison of the charge-carrier dynamics for front and back excitation of the mixed quasi-2D/3D perovskite film. A linear rescaling of the THz photoconductivity transients is demonstrated, to minimise errors arising from the effects of the reflection losses from each side. With this

correction, the THz photoconductivity transients for excitation of the back and front of the mixed quasi-2D/3D perovskite film can be more accurately compared.

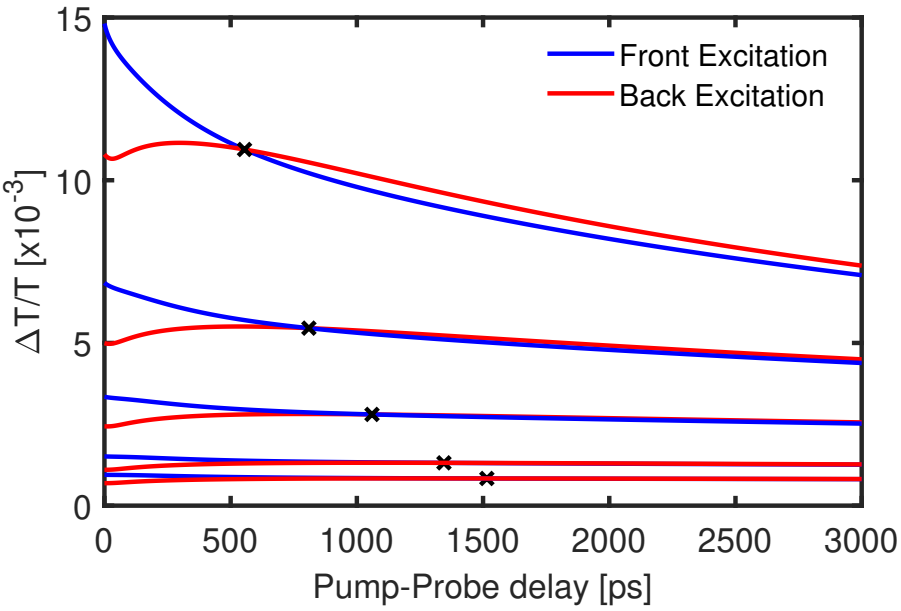

Figure S25: THz photoconductivity transients modelled for the mixed quasi-2D/3D perovskite film, ignoring any reflection losses on either side of the sample and with $k_2 = 6.9 \times 10^{-10}\,\mathrm{cm^3\,s^{-1}}$. The excitation fluences are $16.0\,\mu\mathrm{J\,cm^{-2}}$, $7.4\,\mu\mathrm{J\,cm^{-2}}$, $3.6\,\mu\mathrm{J\,cm^{-2}}$, $1.6\,\mu\mathrm{J\,cm^{-2}}$ and $1.0\,\mu\mathrm{J\,cm^{-2}}$. For each fluence a black cross indicates the time when the THz photoconductivity transients for back and front side excitation are equal (due to the heterogeneous PL, as described in 7).

Before including reflection losses, THz photoconductivity transients for excitation from each side of the mixed quasi-2D/3D perovskite film were simulated, assuming no reflection losses. These THz photoconductivity transients will then serve as a benchmark, to determine how the reflection losses affect the charge-carrier dynamics.

Without reflection losses, for a given pump fluence, there is no difference in the number of charge carriers injected into the back and front of the film. This allows a direct comparison of the differences in charge-carrier dynamics caused by the intrinsic material properties, rather than the in-coupling of different light intensities. Figure S25 shows the THz photoconductivity decays produced by the model in this case. The excitation fluences used are the same as those set in the OPTP study in Section 1.5, and transients are modelled for excitation from the front and back of the film, assuming no reflection losses. A clear pattern

can be observed in the time taken for the THz photoconductivity transients for back and front excitation to cross. Each of the pairs of lines cross, with lower fluence lines taking longer to cross. This provides an idealised set of THz photoconductivity decays for equal excitation of the back and front side of the sample, against which further simulations, which include reflection losses, can be compared.

In the simulations above, the number of charge carriers injected into the back and front of the sample is the same. However, in OPTP experiments, usually only the incident laser power is kept constant between back and front excitations, while the reflection of each side will vary. Comparing the THz photoconductivity dynamics of the two sides is therefore complicated by the fact that the number of charge carriers injected into each side will be slightly different, due to the different reflection losses. At 400 nm the mixed quasi-2D/3D perovskite film, reflected 20% of incident light from the front side and only 6% from the back, as determined using FTIR spectroscopy. What is now required is a means of correcting for these differing reflection losses, so that the dynamics of the two sides can be compared.

In order to determine the effect of the reflection losses for the mixed quasi-2D/3D perovskite film, THz photoconductivity decays were again simulated, using the excitation fluences used in the OPTP study, and accounting for reflection losses. In the model, these reflection losses lower the number of charge carriers initially generated by the pump-pulse. The dotted lines in Figure S26 show the raw THz photoconductivity decays for the top two fluences used in OPTP, accounting for reflection losses. However, as the simulations for back and front excitation initially contain different numbers of charge carriers, it does not make sense to directly compare these raw THz photoconductivity transients.

Instead, the solid lines in Figure S26 show each transient scaled up by a factor of $1/(1-\mathrm{R})$, where R is the pump beam reflection loss off each side. This linear correction for the small difference in excited charge carriers rescales each THz photoconductivity transient to have the same initial value as in Figure S25, where there are no reflection losses. This scaling is equivalent to normalising each THz photoconductivity transient by the number of injected

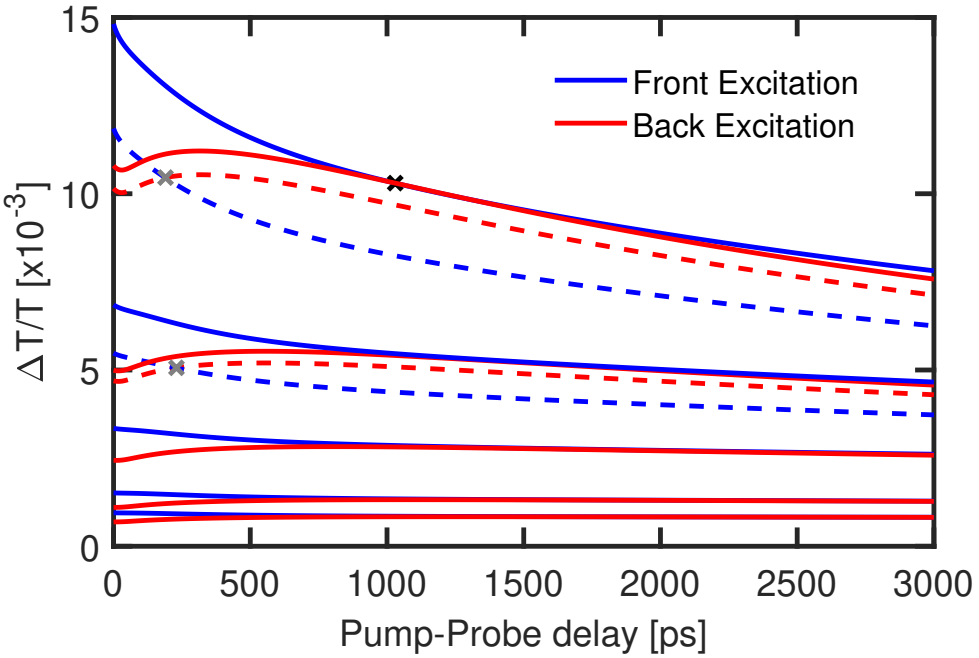

Figure S26: THz photoconductivity transients modelled for the mixed quasi-2D/3D perovskite film, accounting for the reflection losses from each side of the sample and with $k_2 = 6.9 \times 10^{-10}\,\mathrm{cm^3\,s^{-1}}$. At 400 nm, the reflection losses are 0.2 from the front side, and 0.06 from the back side. Dotted lines show the raw THz photoconductivity transients, while the solid lines are scaled by scaled up by a factor of $1/(1 - \mathrm{R})$ to correct for the reflection losses. The excitation fluences are $16.0\,\mu\mathrm{J\,cm^{-2}}$, $7.4\,\mu\mathrm{J\,cm^{-2}}$, $3.6\,\mu\mathrm{J\,cm^{-2}}$, $1.6\,\mu\mathrm{J\,cm^{-2}}$ and $1.0\,\mu\mathrm{J\,cm^{-2}}$. For each fluence, a black cross indicates the time when the corrected THz photoconductivity transients for back and front side excitation are equal, while grey crosses show the crossing points of the raw lines.

charge carriers, as described in the main text. When the scaling is made, the data can be seen to more closely resemble Figure S25 and the trend in crossing times is partially recovered.

The validity of rescaling the reflection-corrected THz photoconductivity transients can be ascertained by directly comparing them with the transients modelled without any reflections. This determines how close rescaled experimental THz photoconductivity transients will be to the case where equal numbers of charge carriers are incoupled into the back and front of the sample. Figure S27 shows a comparison of the THz photoconductivity decays for the lowest excitation fluence shown in Figures S25 and S26. The 'unscaled' transients are modelled with no reflections considered, while the 'scaled' transients consider reflection losses, and are linearly scaled up by $1/(1-R)$ as described above. Because of this rescaling, both the scaled and unscaled THz photoconductivity transients start at the same value. However, in the scaled transients, fewer charge carriers are present in the simulations, as reflection losses are considered. As there are fewer charge carriers, n is lower and the bimolecular recombination is slower than in the unscaled case. This means that when the THz photoconductivity transients are scaled up, they decay more slowly than the equivalent unscaled transients.

In Figure S27, it can be seen that the scaled THz photoconductivity transients (which have been corrected for reflection loss) decay more slowly than the unscaled transients (which are modelled in the absence of any reflection losses). While there is little difference between the scaled and unscaled transients for back excitation, there is a much larger discrepancy for front excitation. This can be explained by the different reflection losses, which were measured as 0.20 for the front side but only 0.06 for the back. As the reflection loss from the front side is larger, so is the difference in the charge-carrier density away from the unscaled case. This larger difference makes the linear correction less accurate for the case of front side excitation.

Although the scaling does not recover the exact shape of the transients, it does closely resemble the unscaled decays. The absolute differences in ΔT/T for the case shown are $O(10^{-5})$, which is an error of around 2.5%. This is within the noise of the OPTP experi-

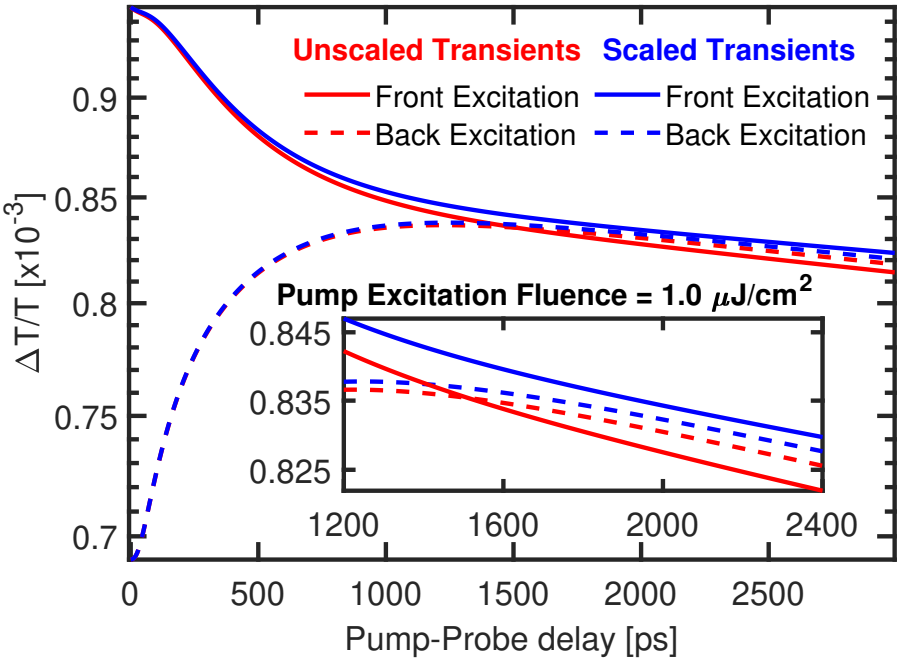

Figure S27: A comparison of THz photoconductivity transients modelled for the mixed quasi-2D/3D perovskite film, for excitation from the back and front sides, with an incident fluence of 1.0 µJ cm^{-2}. Unscaled lines are simulated assuming no reflection losses. The scaled lines account for reflection losses, but in the figure, the simulated THz photoconductivity is shown scaled by a factor of $1/(1-\mathrm{R})$, to correct for the reflection losses. The scaling means that both sets of THz photoconductivity transients have the same initial value of $\Delta T/T$. Note that in both cases the scaling has recovered the initial value of $\Delta T/T$.

ment, and so rescaling the experimental THz photoconductivity transients will not produce a measurable error. At higher fluences bimolecular losses are larger, so the correction will be less accurate, especially for the case of front side excitation. However making a linear correction to the data is still a considerable improvement, especially since the maximum time-delay used in the OPTP experiment is 1.25 ns, rather than the 3 ns time-window shown here.

Therefore, the linear correction procedure outlined here is a valid approximation, which can be used to correct the experimental OPTP transients shown in the main manuscript.

References

(S1) Yang, R.; Li, R.; Cao, Y.; Wei, Y.; Miao, Y.; Tan, W. L.; Jiao, X.; Chen, H.; Zhang, L.; Chen, Q.; Zhang, H.; Zou, W.; Wang, Y.; Yang, M.; Yi, C.; Wang, N.; Gao, F.; McNeill, C. R.; Qin, T.; Wang, J.; Huang, W. *Advanced Materials* **2018**, *30*, 1804771.

(S2) Wehrenfennig, C.; Liu, M.; Snaith, H. J.; Johnston, M. B.; Herz, L. M. *J. Phys. Chem. Lett.* **2014**, *5*, 1300–1306.

(S3) Crothers, T. W.; Milot, R. L.; Patel, J. B.; Parrott, E. S.; Schlipf, J.; Müller-Buschbaum, P.; Johnston, M. B.; Herz, L. M. *Nano Letters* **2017**, *17*, 5782–5789.

(S4) Yuan, M.; Quan, L. N.; Comin, R.; Walters, G.; Sabatini, R.; Voznyy, O.; Hoogland, S.; Zhao, Y.; Beauregard, E. M.; Kanjanaboos, P.; Lu, Z.; Ha Kim, D.; Sargent, E. H. *Nature Nanotechnology* **2016**, *11*, 872.

(S5) Tiwana, P.; Parkinson, P.; Johnston, M. B.; Snaith, H. J.; Herz, L. M. *J. Phys. Chem. C* **2010**, *114*, 1365–1371.

(S6) Pazos-Outon, L. M.; Szumilo, M.; Lamboll, R.; Richter, J. M.; Crespo-Quesada, M.; Abdi-Jalebi, M.; Beeson, H. J.; Vru ini, M.; Alsari, M.; Snaith, H. J.; Ehrler, B.; Friend, R. H.; Deschler, F. *Science* **2016**, *351*, 1430–1433.

(S7) Richter, J. M.; Abdi-Jalebi, M.; Sadhanala, A.; Tabachnyk, M.; Rivett, J. P.; Pazos-Outón, L. M.; Gödel, K. C.; Price, M.; Deschler, F.; Friend, R. H. *Nat. Commun.* **2016**, *7*, 506–514.

(S8) Ahrenkiel, R. K.; Dunlavy, D. J.; Keyes, B.; Vernon, S. M.; Dixon, T. M.; Tobin, S. P.; Miller, K. L.; Hayes, R. E.; Ahrenkie, R. K.; Dunlavy, D. J.; Keyes, B. *Appl. Phys. Lett.* **1989**, *55*, 1088–1090.

(S9) Saliba, M.; Correa-Baena, J.-P.; Grätzel, M.; Hagfeldt, A.; Abate, A. *Angewandte Chemie International Edition* **2018**, *57*, 2554–2569.

(S10) Tress, W. *Advanced Energy Materials* **2017**, *7*, 1602358.

(S11) Jiang, Q.; Zhao, Y.; Zhang, X.; Yang, X.; Chen, Y.; Chu, Z.; Ye, Q.; Li, X.; Yin, Z.; You, J. *Nature Photonics* **2019**, DOI: 10.1038/s41566–019–0398–2.

(S12) Yang, W. S.; Park, B. W.; Jung, E. H.; Jeon, N. J.; Kim, Y. C.; Lee, D. U.; Shin, S. S.; Seo, J.; Kim, E. K.; Noh, J. H.; Seok, S. I. *Science* **2017**, *356*, 1376–1379.